

A 16 deg² survey of emission-line galaxies at $z < 1.6$ from HSC-SSP PDR2 and CHORUS

Masao HAYASHI¹, Rhythm SHIMAKAWA^{1,2}, Masayuki TANAKA^{1,3}, Masato ONODERA², Yusei KOYAMA^{2,3}, Akio K. INOUE^{4,5}, Yutaka KOMIYAMA^{1,3}, Chien-Hsiu LEE⁶, Yen-Ting LIN⁷ and Kiyoto YABE⁸

¹National Astronomical Observatory of Japan, 2-21-1 Osawa, Mitaka, Tokyo 181-8588, Japan

²Subaru Telescope, National Astronomical Observatory of Japan, National Institutes of Natural Sciences, 650 North A'ohoku Place, Hilo, HI 96720, USA

³Department of Astronomy, School of Science, Graduate University for Advanced Studies (SOKENDAI), 2-21-1, Osawa, Mitaka, Tokyo 181-8588, Japan

⁴Department of Physics, School of Advanced Science and Engineering, Waseda University, 3-4-1, Okubo, Shinjuku, Tokyo 169-8555, Japan

⁵Waseda Research Institute for Science and Engineering, 3-4-1, Okubo, Shinjuku, Tokyo 169-8555, Japan

⁶NSFs National Optical-Infrared Astronomy Research Laboratory, USA

⁷Academia Sinica Institute of Astronomy and Astrophysics, PO Box 23-141, Taipei 10617, Taiwan

⁸Kavli Institute for the Physics and Mathematics of the Universe (Kavli IPMU, WPI), The University of Tokyo, 5-1-5 Kashiwanoha, Kashiwa, Chiba 277-8583, Japan

*E-mail: masao.hayashi@nao.ac.jp

Received 2020 March 26; Accepted 2020 July 15

Abstract

We have conducted a comprehensive survey of emission-line galaxies at $z \lesssim 1.6$ based on narrowband (NB) imaging data taken with Hyper Suprime-Cam (HSC) on the Subaru telescope. In this paper, we update the catalogs of H α , [OIII], and [OII] emission-line galaxies using the data from the second Public Data Release (PDR2) of Subaru Strategic Program (SSP) of HSC and Cosmic HydrOgen Reionization Unveiled with Subaru (CHORUS) survey along with the spectroscopic redshifts for 2,019 emission-line galaxies selected with the PDR1 data. The wider effective coverage of NB816 and NB921, 16.3 deg² and 16.9 deg² respectively, are available in the Deep and UltraDeep layers of HSC-SSP from the PDR2. The CHORUS survey provides us with data with additional three NBs (NB527, NB718, and NB973) in the COSMOS field in the UltraDeep layer (1.37 deg²). The five NB datasets allow us to investigate the star-forming galaxies presenting emission-lines at 14 specific redshifts ranging from $z \sim 1.6$ down to $z \sim 0.05$. We revisit the distribution of large-scale structures and luminosity functions (LFs) for the emission-line galaxies with the large samples of 75,377 emission-line galaxies selected. The redshift revolution of LFs shows that the star formation rate densities (SFRDs) decreases monotonically from $z \sim 1.6$, which is consistent with the cosmic SFRD ever known. Our samples of emission-line galaxies covering a sufficiently large survey volume are useful to investigate the evolution of star-forming galaxies since the cosmic noon in a wide range of environments including galaxy clusters, filaments, and voids.

Key words: galaxies: evolution — galaxies: high-redshift — galaxies: luminosity function, mass function — large-scale structure of universe

1 Introduction

Our global understanding of evolution of star-forming galaxies has reached a consensus; the cosmic star formation rate (SFR) density peaks at $z = 1\text{--}3$ and then gradually declines towards the local Universe (e.g., Hopkins & Beacom 2006; Madau & Dickinson 2014). It is also well-known that star-forming galaxies maintain a tight correlation between SFR and stellar mass from $z \sim 6$ all the way to the local Universe, while SFR at a given stellar mass becomes lower at decreasing redshifts (e.g., Daddi et al. 2007; Elbaz et al. 2007; Noeske et al. 2007; Speagle et al. 2014; Whitaker et al. 2014; Tomczak et al. 2016). However, physics governing the evolution of the activity in individual star-forming galaxies is not yet fully understood. Given that a fraction of quiescent galaxies is dependent on both stellar mass and environment (e.g., Peng et al. 2010) and there is a small fraction of galaxies in a starburst phase (e.g., Rodighiero et al. 2011), star-formation history of individual star-forming galaxies is complicated. In order to reveal the contribution of each process stimulating and/or quenching star-formation activity to the evolution of the individual galaxies, first of all, it is essential to conduct a comprehensive survey of star-forming galaxies at the redshifts $z \lesssim 3$ that covers a wide range in terms of star formation activity, stellar mass and environment.

Narrowband (NB) imaging is effective in surveying star-forming galaxies with nebular emission lines at a specific redshift in a homogeneous field-of-view (FoV) without any bias for target selection. The distribution of emission-line galaxies selected is insensitive to the projection effect thanks to small redshift ranges surveyed by NB imaging. Therefore, a large sample of emission-line galaxies is useful to investigate the properties of star-forming galaxies as well as the dependence of galaxy properties on environment in each specific redshift surveyed (e.g., Ly et al. 2007; Ly et al. 2011; Ly et al. 2012; Lee et al. 2012; Dale et al. 2010; Drake et al. 2013; Sobral et al. 2009; Sobral et al. 2011; Sobral et al. 2012; Sobral et al. 2013; Sobral et al. 2014; Sobral et al. 2015; Sobral et al. 2016a; Sobral et al. 2016b; Khostovan et al. 2015; Khostovan et al. 2016; Khostovan et al. 2018; Khostovan et al. 2020; Matthee et al. 2017; Stroe et al. 2014; Stroe et al. 2015; Stroe & Sobral 2015; Stroe et al. 2017b; Hayashi et al. 2015; Hayashi et al. 2018; Koyama et al. 2018; Coughlin et al.

2018; Harish et al. 2020; Bongiovanni et al. 2020; Ramón-Pérez et al. 2019a; Ramón-Pérez et al. 2019b; Nadolny et al. 2020). However, a wide-field imaging is required to survey a volume large enough so that galaxy properties investigated are independent of cosmic variance. The $\sim 10 \text{ deg}^2$ NB imaging surveys by Sobral et al. (2015) and Stroe & Sobral (2015) show that a large survey volume of $>3.5\text{--}5.0 \times 10^5 \text{ Mpc}^3$ can overcome cosmic variance and then the luminosity functions of emission-line galaxies are derived with an error of $< 10\%$. From a theoretical point of view, Ogura et al. (2020) investigate the influence of the field variance in $\text{H}\alpha$ emission-line galaxies at $z = 0.4$ using a semi-analytic model for the galaxy formation, the New Numerical Galaxy Catalog ($\nu^2\text{GC}$), and find that a survey area of more than 15 deg^2 is required to restrict the uncertainties in the luminosity functions of $\text{H}\alpha$ emitters at $z = 0.4$ to less than $\sim 10\%$.

The Subaru Strategic Program (SSP) with Hyper Suprime-Cam (HSC) provides us with the data useful for the study of galaxy evolution. The HSC-SSP is an ongoing survey since 2014 (Aihara et al. 2018b), and the deep imaging is conducted in five broadband (BB) filters: *grizy*, plus four NB filters: NB387, NB816, NB921, and NB1010 (figure 1) in the Deep (D) and UltraDeep (UD) layers over 28 deg^2 in total. The HSC is an instrument on the 8.2-m Subaru Telescope with the capability to cover 1.77 deg^2 in a single pointing (Miyazaki et al. 2018; Komiyama et al. 2018; Kawanomoto et al. 2018; Furusawa et al. 2018). In addition to the wide FoV and good image quality of the data, an assortment of many NB filters is one of the uniqueness of HSC. Since the dataset of the HSC-SSP is huge, constructing catalogs of emission-line galaxies in a consistent manner is crucial for systematic studies of galaxy evolution.

The first public data release (PDR1) of HSC-SSP data was published on 2017 February 28 (Aihara et al. 2018a). Hayashi et al. (2018) use the data from two NB filters, NB816 and NB921, available in the PDR1 of HSC-SSP to search for galaxies with nebular emission of $\text{H}\alpha$, $[\text{OIII}](\lambda\lambda = 4960, 5008\text{\AA})$, or $[\text{OII}](\lambda\lambda = 3727, 3730\text{\AA})$ at $z \lesssim 1.5$. Since the NB816 (NB921) data cover 5.7 (16.2) deg^2 area, the HSC-SSP survey provides us with one of the largest samples of emission-line galaxies at $z < 1.5$ ever constructed. The catalogs¹ include 8054 $\text{H}\alpha$ emitters at $z \approx$

¹ The catalogs are available in <https://hsc-release.mtk.nao.ac.jp/>.

0.25 and 0.40, 8656 [OIII] emitters at $z \approx 0.63$ and 0.84, and 16877 [OII] emitters at $z \approx 1.19$ and 1.47. The spatial distribution of the emitters shows large-scale structures over $\gtrsim 50$ Mpc region that consist of star-forming galaxies in various environments covering from cores of galaxy clusters to voids (Hayashi et al. 2018; Koyama et al. 2018). Thanks to the large survey volume of more than 5×10^5 Mpc³, the luminosity functions of the emitters overcome the field-to-field variance and are determined with small uncertainty.

However, since the survey is not completed yet as of the PDR1, there remains room for improvement in search for emission-line galaxies. Only data from two NBs are available in the PDR1, and the field coverage of NB816 data (5.7 deg²) is limited to one-third of NB921 data (16.2 deg²). Furthermore, we realize that the PDR1 catalogs of emission-line galaxies are biased towards galaxies with large equivalent width (EW) of nebular emission line, compared with the other deep surveys (Ly et al. 2007; Sobral et al. 2013); an observed EW of 48Å for NB816 emitters and 56Å for NB921 emitters, respectively. Ly et al. (2007) selected NB816 and NB921 emitters with the observed EWs of >33 and >15 Å, respectively. Sobral et al. (2013) selected NB921 emitters with the rest-frame EWs greater than 25 Å, namely the H α emitters with smaller EWs were selected compared with the PDR1 catalog.

The second public data release (PDR2) of HSC-SSP data was published on 2019 May 31 (Aihara et al. 2019). The NB data from the PDR2 are deeper and wider than the PDR1 data. The data with three other NB filters (NB527, NB718, and NB973) are also available in the UD-COSMOS field (1.7 deg²) from the Subaru open-use intensive program named Cosmic HydrOgen Reionization Unveiled with Subaru (CHORUS, Inoue et al. 2020). We have conducted follow-up spectroscopic campaigns and confirmed about 2000 emission-line galaxies selected from the PDR1 data. Based on the newly available imaging data as well as the spectroscopic data, we aim to update the catalogs of emission-line galaxies at $z \lesssim 1.6$ in this study. The deeper and wider data allow us to select more representative star-forming galaxies in a wide range of environments covering rare ones in high or low density regions. With the catalogs, we can investigate the redshift evolution of star-formation activity of star-forming galaxies and large-scale structures.

The outline of this paper is as follows. In § 2, the NB data from HSC-SSP PDR2 and CHORUS surveys as well as the spectroscopic data from the follow-up observations

The name of the catalogs is `pdr1.udeep.nbemitter` for emission-line galaxies in the fields of UltraDeep layer and `pdr1.deep.nbemitter` for those of Deep layer.

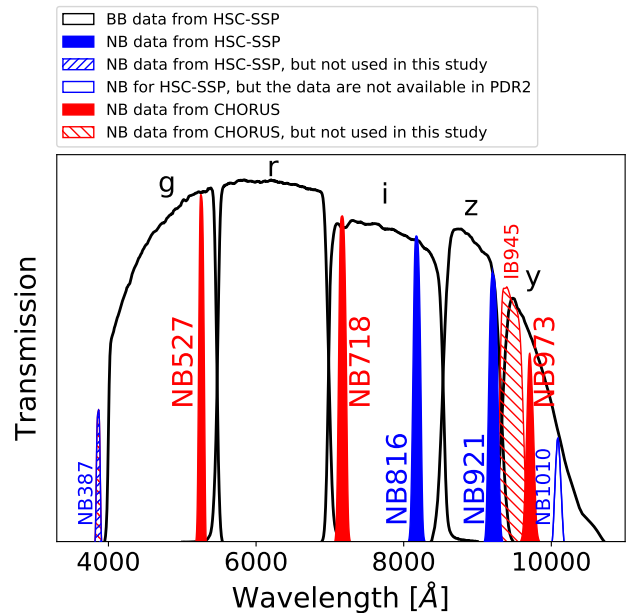


Fig. 1. The set of broadband (BB) and narrowband (NB) filters used in the HSC-SSP and CHORUS surveys. The response function of the filters and the quantum efficiency of CCD are taken into account for the transmission. The transmission curves in blue show the NB filters used in the HSC-SSP, while the red ones are used in the CHORUS survey. The data from the filled NB filters are used in this study. The data from the open NB filter is not available in the PDR2. The data from the hatched filters are not used in this study (see the text for the details), although the data are available.

of the PDR1 galaxies are described. Emission-line galaxies at $z \lesssim 1.6$ are selected in § 3, and we mention therein how we improve the selection of emission-line galaxies. In § 4, luminosity functions of the emission-line galaxies are investigated. We discuss the redshift evolution of the luminosity functions and the cosmic star formation rate densities by integrating the luminosity functions in § 5. Finally, conclusions are given in § 6. Throughout this paper, magnitudes are presented in the AB system (Oke & Gunn 1983). The cosmological parameters of $H_0 = 70$ km s⁻¹ Mpc⁻¹, $\Omega_m = 0.3$ and $\Omega_\Lambda = 0.7$, along with Chabrier (2003) initial mass function (IMF), are adopted.

2 Data

2.1 HSC imaging data

We use the data from five NB filters, NB527, NB718, NB816, NB921, and NB973 (see also figure 1), taken through the HSC-SSP and CHORUS programs. Table 1 summarizes the NB data we use in this study. The BB data are all from the HSC-SSP PDR2.

Table 1. The NB filters used in this study. The area shows the effective area that is not masked with the flags we apply and bright object masks (§ 2.1.1). The depth is 5σ limiting magnitude in the representative 9 patch regions of each field (see table 2), which is measured from a standard deviation of 2 arcsec aperture photometry in random sky positions in the image with PSF matched to 1.1 arcsec.

NB filter	λ_c (Å)	$\Delta\lambda$ (Å)	AREA [†] (deg ²)	Deep / UltraDeep layer							
				SXDS+XMM-LSS		COSMOS		ELAIS-N1		DEEP2-3	
				area (deg ²)	depth [‡] (mag)	area (deg ²)	depth [‡] (mag)	area (deg ²)	depth (mag)	area (deg ²)	depth (mag)
NB527*	5261	79	1.37 (1.76)	–	–	1.37 (1.76)	26.32	–	–	–	–
NB718*	7170	111	1.37 (1.76)	–	–	1.37 (1.76)	25.61	–	–	–	–
NB816	8177	113	16.28 (21.02)	5.16 (6.34)	25.43	1.37 (1.76)	25.58	4.79 (6.42)	24.90	4.97 (6.49)	24.82
NB921	9214	135	16.79 (22.09)	1.32 (1.76)	25.25	5.78 (7.50)	25.39	4.79 (6.42)	24.76	4.91 (6.41)	24.59
NB973*	9711	108	1.37 (1.76)	–	–	1.37 (1.76)	24.63	–	–	–	–

* The data are from CHORUS survey, otherwise the data are from HSC-SSP.

[†] The area in parenthesis shows the area before masking with bright object masks.

[‡] In the SXDS+XMM-LSS and COSMOS fields, the depth is measured in the UD layer.

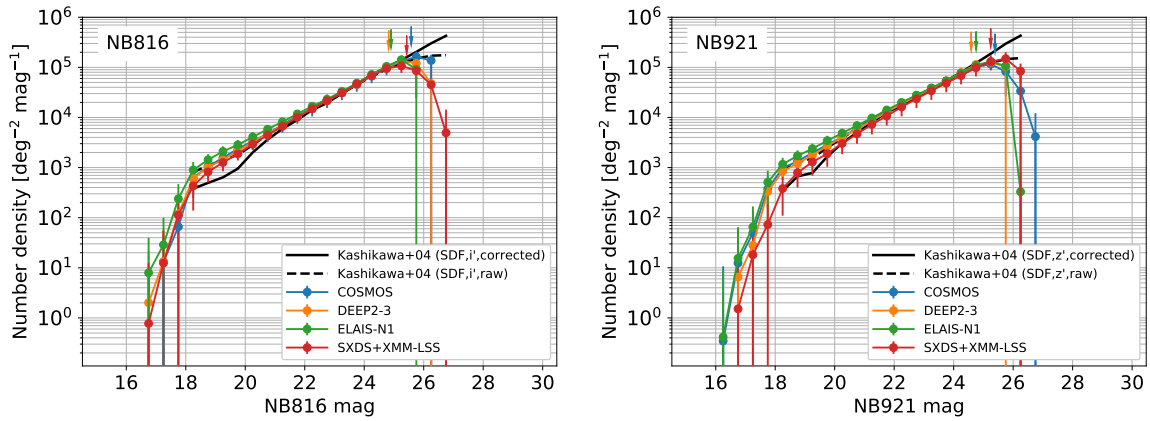


Fig. 2. The number counts of sources detected in NB816 or NB921, namely stars and galaxies are all included. The horizontal axis is convolvedflux_2.20_mag, which is magnitude by 2 arcsec aperture photometry on the images with PSF matched to 1.1 arcsec. The number counts are corrected for detection completeness and only the sources with more than 50% of detection completeness are used for the plots. The symbols in different colors show the number counts in each four field. The error bars show the standard deviation of the number counts in individual patch regions. The black lines are from the literature (Kashikawa et al. 2004), where the dashed line is the number count of all sources. The arrows show the 5σ limiting magnitudes.

Table 2. Representative regions in each field used for calculation of detection completeness and 1σ sky noise.

D/UD	field	tract	patch
UltraDeep	SXDS	8523	105,106,107,205,206,207,305,306,307
UltraDeep	COSMOS	9813	303,304,305,403,404,405,503,504,505
Deep	XMM-LSS	8524	203,204,205,303,304,305,403,404,405
Deep	E-COSMOS	9814	606,607,608,706,707,708,806,807,808
Deep	ELAIS-N1	17271	405,406,407,505,506,507,605,606,607
Deep	DEEP2-3	9464	402,403,404,502,503,504,602,603,604

2.1.1 SSP public data release 2

The HSC-SSP PDR2 publishes the data observed with 174 nights between March 2014 and January 2018 (Aihara et al. 2019). The PDR2 is equivalent to the internal S18A release for the HSC-SSP collaboration. Among the four NB filters planned in the HSC-SSP, NB387 data are newly available in this release, while NB1010 data are not yet, but will be available in the next release, i.e., PDR3. The

coverage of NB816 and NB921 data that are already available in the PDR1 increases to be 26 deg² covered by the Deep layer, where the NB data are available, consists of four separate fields: XMM-LSS, E-COSMOS, ELAIS-N1, and DEEP2-3. Among them, XMM-LSS and E-COSMOS fields each encompasses the UltraDeep layer covered by a single pointing of HSC, which are named SXDS and COSMOS, respectively. Note that the UD-COSMOS in the UD layer is similar to the well-known COSMOS field (Scoville et al. 2007), and the E-COSMOS in the D layer is a extended field around the original COSMOS. Unless specifically mentioned, we use “COSMOS” as a field covering the extended area around the original COSMOS field in this paper, because the data in both UD-COSMOS and E-COSMOS are jointly processed and cataloged. In this study, we use the NB816 and NB921 data from the HSC-

SSP, because only [OII]($\lambda = 3727, 3730\text{\AA}$) from galaxies at $z \sim 0.038$ can enter the NB387 filter among strong nebular emission lines of H α , [OIII], and [OII] we focus on now and the redshift is too low to get enough survey volume. Also, it is difficult to estimate the stellar continuum level underlying emission lines at the wavelength of NB387 with only the HSC BB filters (figure 1). The u -band data are essential to select emission-line galaxies detected in NB387 (Nakajima et al. 2012; Konno et al. 2016; Sobral et al. 2017; Stroe et al. 2017a).

The HSC-SSP PDR2 data are processed with the pipeline, `hscPipe` version 6 (Bosch et al. 2018; Aihara et al. 2019), which includes the data reduction, source detection, and photometry. Readers should refer to Bosch et al. (2018) for the details of the pipeline and to Aihara et al. (2019) for improvements, new features, and remaining issues specific to this version of `hscPipe`. The most notable points closely related to this study are the improvement of sky subtraction and joint processing of the data in the D and UD layers. Note that in the PDR1, the data in the COSMOS and SXDS+XMM-LSS fields were processed separately for the D and UD layers, although there are overlapped regions between the two layers. As with the data in the PDR1, the survey area is divided into predefined gridded regions known as `tract`, each covering $\sim 1.7 \times 1.7\text{deg}^2$. A single `tract` is divided into 9×9 sub-regions, each one called a `patch` and covering $\sim 12 \times 12\text{arcmin}^2$.

The source catalogs in individual D/UD fields are extracted from the Catalog Archive Server (CAS) of the HSC-SSP. To select NB921-detected sources, we apply the following criteria in SQL query:

```
forced.isprimary=True,
meas.(g,r,i,z,y,n921)_inputcount_flag_noinputs=False,
meas.(g,r,i,z,y,n921)_inputcount_value>2,
meas.merge_peak_n921=True,
meas2.n921_sdsshape_flag_badcentroid=False,
meas.(z,n921)_pixelflags_bad=False,
meas.(z,n921)_pixelflags_edge=False,
meas.(z,n921)_pixelflags_saturatedcenter=False,
meas.n921_cmodel_flag=False,
meas2.n921_psfflux_flag=False,
meas2.n921_psfflux_flag_badcentroid=False,
meas2.n921_psfflux_flux!='NaN',
meas2.n921_psfflux_flux/meas2.n921_psfflux_fluxsigma>=5.0,
masks.(g,r,i,z,y)_mask_s18a_bright_objectcenter=False.
```

For NB816-detected sources, we use `i`-band and `n816` for a combination of BB and NB.

The flag of bright object mask applied in the extraction of sources from the CAS is from the revised masks which are released as part of the incremental release 1 (see sec-

tion 6.6.2 of Aihara et al. 2019 as well as Coupon et al. 2018). However, we find that the size of masks for bright stars is not large enough to remove false detections around the prominent stellar haloes. As a workaround, we enlarge a size of masked region around the bright stars by a factor of 1.5, if the original size of masked region is more than 3.0 arcmin in radius. Otherwise, we use the original masked regions around the other stars. The appropriate masked regions are essential not only to remove the spurious objects but also to calculate the proper area and volume for investigating the number counts and luminosity functions of the galaxies selected. We use the catalog of random points (one of the value-added products of HSC-SSP PDR2, see the section 5.4 of Aihara et al. 2019) to calculate the effective survey area in each field, where the random points within the mask regions modified are removed. The results are summarized in table 1.

To validate the source detection in the PDR2, we investigate the number counts of sources detected in NB816 or NB921 (figure 2). The figure shows that the number densities of NB-detected sources including stars and galaxies are consistent with the previous studies (Kashikawa et al. 2004). We use `convolvedflux_2.20_mag`, which is the 2-arcsec aperture photometry on the images with point spread function (PSF) matched to 1.1 arcsec. Note that the number counts are corrected for detection completeness and only the sources with more than 50% of detection completeness are used for the plots. The detection completeness are estimated by running the `hscPipe` on the images where synthetic objects with a PSF profile are embedded in the position of `sky objects`² and then calculating the recovery rate of the embedded synthetic objects with magnitudes ranging from 18.0 to 28.0 mag. We investigate the detection rate for the synthetic objects with magnitude bins of width 0.5 mag. Because doing the analysis in all regions is too time-consuming and unrealistic, we perform the measurements in nine representative `patch` regions in each field; the list of `patch` regions is shown in table 2. The figure 3 shows the detection completeness as a function of magnitude.

The limiting magnitudes in each band are estimated from the photometric errors in the catalogs. However, we find that the absolute values of the photometric errors output by `hscPipe` are underestimated, while the relative values among the objects seem to be valid. Therefore, we rescale the photometric errors to match with the 1σ sky noise. The 1σ sky noise is estimated by fitting a Gaussian profile to the distribution of the flux densities at the ran-

² These are for the measurements on the blank sky position, which can be extracted from the CAS by applying the flag of `merge_peak_sky=True`. See the section 6.6.8 of Aihara et al. 2019.

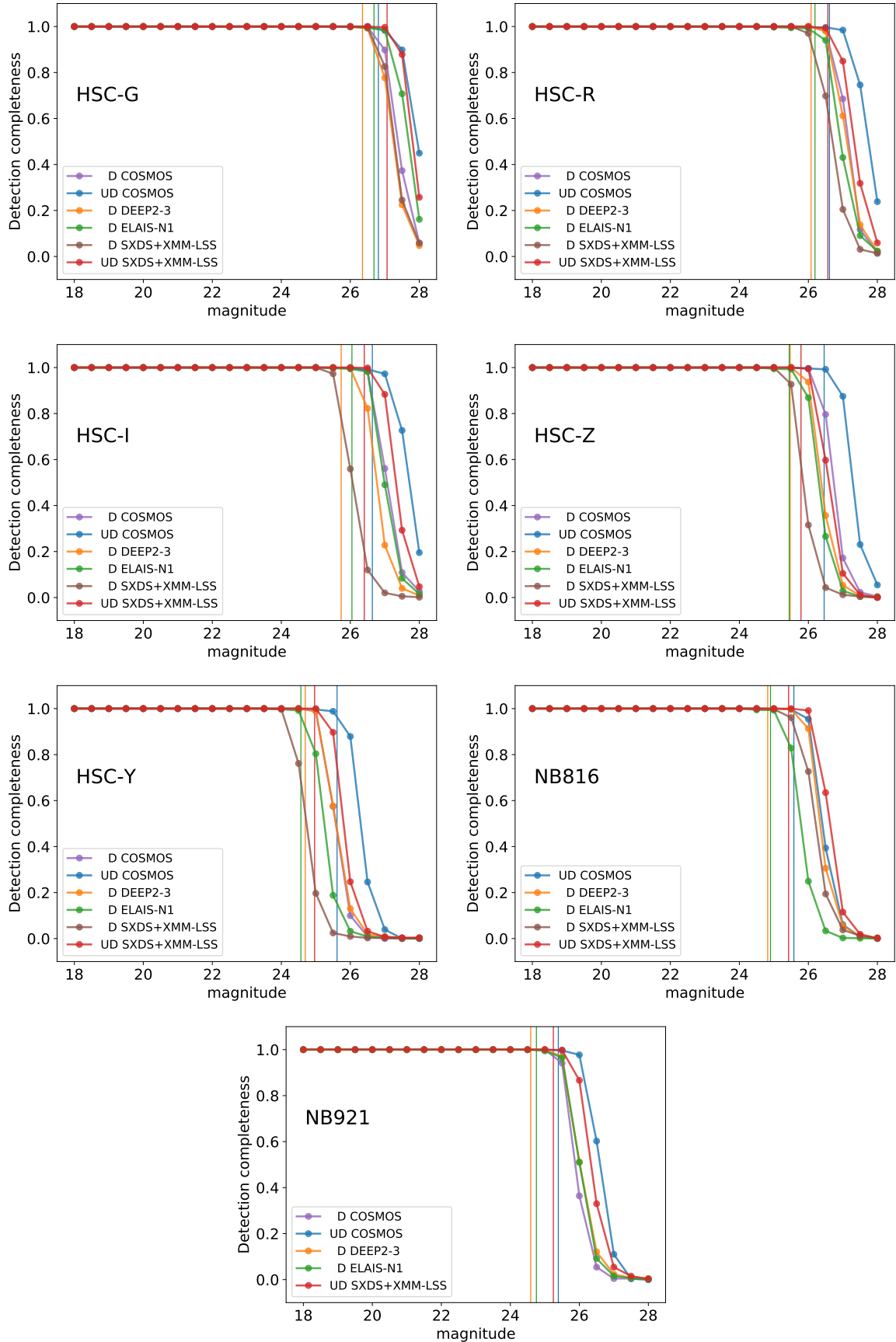


Fig. 3. Detection completeness for five BBs, NB816 and NB921 filters. The vertical lines show the 5σ limiting magnitudes which are measured from the random photometry with 2 arcsec aperture in sky region (see text for the details). For the COSMOS and SXDS+XMM-LSS fields, the 5σ limiting magnitudes are measured in the UltraDeep region. The magnitudes where a detection completeness starts to drop are consistent with the 5σ limiting magnitudes.

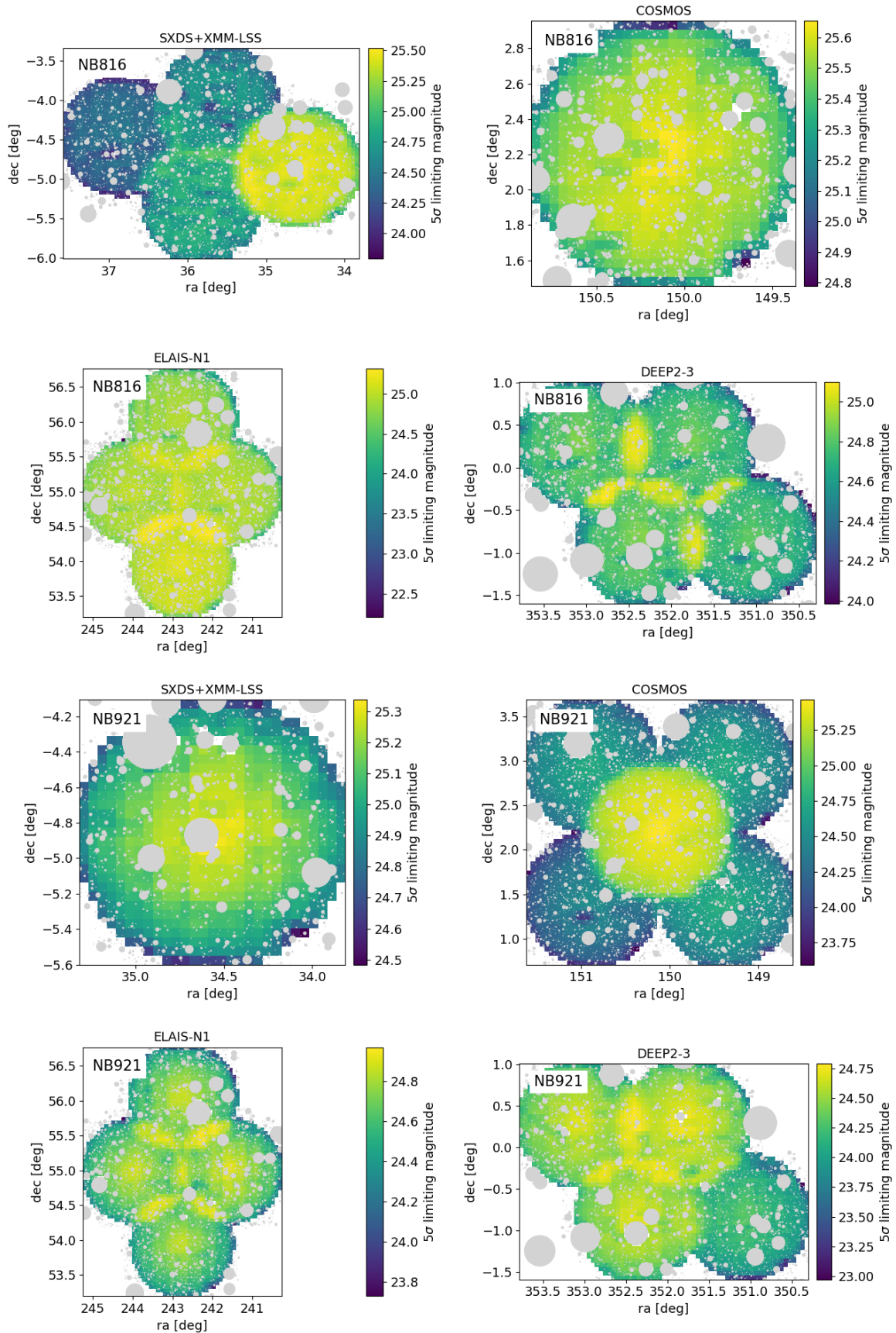


Fig. 4. The map of 5 σ limiting magnitudes in NB816 and NB921. The gray regions are masked for bright objects. The flux density errors in 2 arcsec aperture photometry on the images with PSF matched to 1.1 arcsec are used for the estimate of limiting magnitude.

dom sky positions. The measurements at the sky position are stored as `sky objects` in the CAS. The 5σ limiting magnitudes measured by this method are consistent with the magnitude where the number count is bent or the detection completeness starts to steeply decrease towards zero (see figures 2 and 3). This shows that rescaling the photometric errors is valid. Figure 4 shows the map of 5σ limiting magnitudes of the individual NB data in each field.

2.1.2 CHORUS

CHORUS is a Subaru open-use intensive program (S16B-001I, PI: A. K. Inoue) supplemented with a normal program (S18B-004) to use 14.6 nights in total between 2017 January and 2018 December to conduct HSC imaging with four NB and one intermediate-band filters (NB387, NB527, NB718, IB945, and NB973) in the HSC-SSP UD-COSMOS field. The main science of the CHORUS project is to understand reionization of the Universe at $z > 3$. Therefore, deep NB imaging data are available from this survey. As by-products, the deep data are useful to search for emission-line galaxies at relatively lower redshifts of $z \lesssim 1.6$. Readers should refer to Inoue et al. (2020) for the details of the CHORUS survey such as survey design, observing runs, data quality, and data release. Among the five filters available from the CHORUS survey, we use the data from three filters of NB527, NB718, and NB973 in this study. This is because the same things for the HSC-SSP NB387 apply to the CHORUS NB387 and response function of IB945 is a factor of ~ 3 wider than the other NB filters (324\AA).

The data reduction, source detection, and photometry are conducted with `hscPipe` version 6 in the same manner as the HSC-SSP. Since the data and catalogs from the CHORUS survey are stored in the database of the HSC-SSP internal release, the extract of NB-detected sources from the CAS, the mask of the survey area, measurements of detection completeness, and rescaling the photometric errors are also carried out in the same manner as the HSC-SSP. Although Inoue et al. (2020) also perform the similar validation, we notice that the methods Inoue et al. (2020) apply are slightly different from ours. To keep consistency between the NB data from HSC-SSP and CHORUS surveys within this study, it would be worth showing the results in this paper. The number counts, the detection completeness, and the map of 5σ limiting magnitudes are shown in appendix (figures 18–20).

2.2 Spectroscopic data

2.2.1 Literature

The HSC-SSP CAS contains a catalog of public spectroscopic redshifts collected from literature³, which is one of the value-added products of HSC-SSP PDR2. The catalog of public spectroscopic redshifts is updated since the PDR1. Among the redshifts, we use only the secure ones with a flag of `specz_flag_homogeneous = True` in this study (see the section 5.4 of Aihara et al. 2019), where 73 (98)% of the galaxies with the public spectroscopic redshifts have *i*-band magnitudes brighter than 22.5 (24.0). In addition, we use the spectroscopic redshifts from the Keck/DEIMOS survey in the COSMOS field, which are given by Hasinger et al. (2018).

2.2.2 Subaru/FOCAS

We have confirmed 86 emission-line galaxies by spectroscopy with Subaru/FOCAS (Kashikawa et al. 2002), which were observed in the three programs: 44 NB921 emission-line galaxies (19 in the COSMOS field and 25 in the ELAIS-N1 field) and 28 photo-*z*/color selected galaxies (these are filler targets in COSMOS) are confirmed by the observing run on 14–15 March 2017 (S17A-083, PI: M. Hayashi), 9 galaxies (4 NB816 emitters and 5 NB921 emitters) in the DEEP2-3 field are confirmed by the observing run in September 2016 (S16B-029, PI: T. Shibuya, Shibuya et al. 2018), and 5 NB921 emitters (four in COSMOS and one in ELAIS-N1) are confirmed by the run in March – May 2017 (S16B-071I, PI: Y. Matsuoka, Matsuoka et al. 2018). For our own run (S17A-083), we use 300R grism + SO58 order cut filter. The sky condition in the run on 14 March 2017 was good. Although there were thin clouds over the sky on 15 March 2017, we were able to obtain the spectra. The seeing ranges from 0.60 to 0.79 arcsec.

We reduce the data in the standard manner using `FOCASRED` which is the `IRAF` scripts package for the Subaru/FOCAS data reduction. The reduction procedures are basically the same procedures as described in Hayashi et al. (2019). The details of the other two observations and their data reduction are described in these papers (Shibuya et al. 2018; Matsuoka et al. 2018), respectively.

The redshifts are determined by fitting a Gaussian profile to the emission lines detected in the 1-D spectra. Among the 86 galaxies confirmed, multiple emission lines

³ zCOSMOS DR3 (Lilly et al. 2009), UDSz (Bradshaw et al. 2013; McLure et al. 2013), 3D-HST (Skelton et al. 2014; Momcheva et al. 2016), FMOS-COSMOS (Silverman et al. 2015; Kashino et al. 2019), VVDS (Le Fèvre et al. 2013), VIPERS PDR1 (Garilli et al. 2014), SDSS DR12 (Alam et al. 2015), the SDSS IV quasi-stellar object catalog (Pâris et al. 2018), GAMA PDR2 (Liske et al. 2015), WiggleZ DR1 (Drinkwater et al. 2010), DEEP2 DR4 (Davis et al. 2003; Newman et al. 2013), DEEP3 (Cooper et al. 2011; Cooper et al. 2012), and PRIMUS DR1 (Coil et al. 2011; Cool et al. 2013).

are detected from 73 galaxies, whose spectroscopic redshifts are robust. Although the other 13 galaxies have a single line detected in the individual spectra, we identify the galaxies with assistance of the photometric redshifts and colors.

2.2.3 AAT/AAOmega+2dF

Most of the spectroscopic confirmation are performed by the Multi-Object Spectroscopy (MOS) observations on 2018 November 10–14 with AAOmega+2dF (Sharp et al. 2006; Lewis et al. 2002) on the Anglo-Australian Telescope (AAT). The AAOmega+2dF has 400 fibers in 2 degree FoV and the light from objects through the fibers is fed to the blue and red arms with a dichroic mirror. We use the 580V grating for blue and 385R grating for red. Since we set the dichroic wavelength to 670nm, the spectra covering 4500–9800Å are simultaneously obtained. We target NB816 or NB921-selected emission-line galaxies in the SXDS field as well as H α emitters at $z \sim 0.4$ in the DEEP2-3 field. The targets are basically selected from the PDR1 catalog, and supplemented from the PDR1 emitter candidates with lower equivalent width of emission line. We give higher priority to galaxies with larger emission line flux. As a result, we observed more than 3000 galaxies with NB-detected line fluxes of $> 4.5 \times 10^{-17}$ erg s $^{-1}$ cm $^{-2}$ (362 H α emitters at $z = 0.25/0.40$, 907 [OIII] emitters at $z = 0.63/0.84$, and 1,418 [OII] emitters at $z = 1.19/1.47$) in the SXDS field, which is a complete sample down to the line flux of $\gtrsim 1.0 \times 10^{-16}$ erg s $^{-1}$ cm $^{-2}$ in the surveyed volume at each redshift. Among the five nights allocated, it was clear sky for three nights. We observed 8 fiber configurations in the SXDS field and 2 configurations in the DEEP2-3 field. The integration time is 80 – 120 min, depending on the fiber configurations.

The spectra are reduced in the standard manner by the pipeline `2dfr` version 6.46, while referring to the procedures in the Australian Dark Energy Survey (OzDES, Yuan et al. 2015). Only the information of redshifts is required from the spectra to identify the NB-selected emission-line galaxies in this study. More details of the spectra will be described in a forthcoming paper where the spectroscopic properties of the emitters are discussed.

To confirm the NB-selected emission-line galaxies, we first search for the emission lines in the wavelength range covered by individual NB filters. Then, to determine the redshifts, we search for other emission lines in the individual spectra. When the multiple emission lines are detected at more than 3σ , the redshifts are determined and thus secure. If a single emission line are detected, we identify the emission line with assistance of the photometric redshifts and colors. Note that the gratings used in the

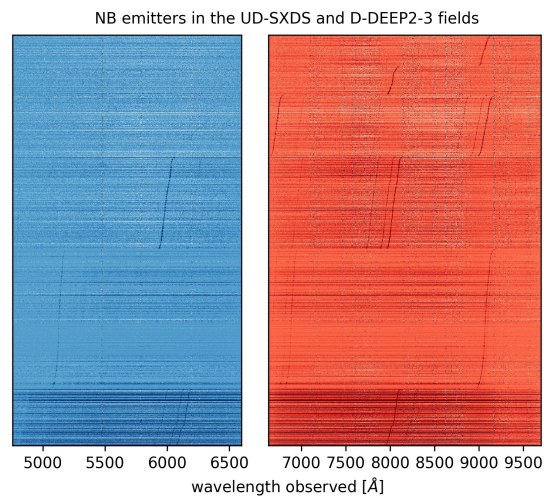


Fig. 5. The AAOmega spectra of the confirmed NB816 and NB921 emitters that are selected from the HSC-SSP PDR1 data. The left shows the spectra in blue arm and the right shows the spectra in red arm. The spectra are lined up in the order of redshift.

observations do not have the spectral resolution enough to resolve the [OII] doublet and the [OII] emitters are expected to have the only single line detected in the wavelength covered by NB filter. We have confirmed 1933 emitters, indicating 64% of success rate. Although some objects can be contaminants among the remaining 36% of the targets, many of the objects that are not confirmed by the spectroscopy are likely to have emission lines less than the detection limit of this observation. Indeed, if we focus on the emitters with emission lines brighter than 1.0×10^{-16} erg s $^{-1}$ cm $^{-2}$, which is likely above the sensitivity expected from the integration time, the success rate increases to more than 80%. Since 554 confirmed galaxies also have the spectroscopic redshifts from the literature, we compare the redshifts from the AAOmega spectra with those from the literature. The median of the difference is $(\Delta z)_{\text{median}} = -4.90 \times 10^{-4}$ and the dispersion is $\sigma(\Delta z) = 6.32 \times 10^{-3}$, suggesting that there is no systematic difference in the redshifts and both redshifts are consistent with each other. Figure 5 shows the spectra taken with AAT/AAOmega+2dF.

3 Emission-line galaxies

The procedures to select and identify emission-line galaxies are basically the same as those for the PDR1 data in Hayashi et al. (2018). However, we change several points to adjust to the PDR2 data. In this paper, we focus on the difference from the PDR1. We survey emission-line galaxies at the 14 redshift slices as shown in table 3. As with the PDR1 catalogs, the catalogs of the emission-line galaxies

Table 3. Redshifts of emission-line galaxies surveyed with the NB filters.

redshift	redshift range	line	NB
0.050	0.042 – 0.058	[OIII]	NB527
0.092	0.084 – 0.101	H α	NB718
0.246	0.237 – 0.254	H α	NB816
0.404	0.393 – 0.414	H α	NB921
0.411	0.400 – 0.422	[OII]	NB527
0.432	0.421 – 0.443	[OIII]	NB718
0.479	0.471 – 0.488	H α	NB973
0.633	0.621 – 0.644	[OIII]	NB816
0.840	0.826 – 0.853	[OIII]	NB921
0.923	0.908 – 0.938	[OII]	NB718
0.939	0.928 – 0.950	[OIII]	NB973
1.193	1.178 – 1.208	[OII]	NB816
1.471	1.453 – 1.489	[OII]	NB921
1.605	1.590 – 1.619	[OII]	NB973

made in this paper will be released at the HSC-SSP data release site⁴. The catalog from the HSC-SSP NB data will be released soon after the paper is published. The catalog from the CHORUS data will be also released at the same time as or after the CHORUS NB data are published.

3.1 Selection

We use the NB data as well as all of the BB data to select emission-line galaxies. We change the method of photometry from the model fitting with two components (`cmodel` magnitude) to the fixed aperture (`undeblended_convolvedflux_2.11` magnitude) to measure the color excess against a photometric error in BB – NB color at a given NB magnitude. The aperture photometry is a measurement of flux density for each object on the PSF matched coadd images, where the target PSF is 1.1 arcsec and the aperture size is 1.1 arcsec. Note that the photometry is conducted on the undeblended images, namely the detected footprints are not deblended into each object. This is because we found that there are some objects having `cmodel` magnitudes unnaturally bright, which could be in part due to failure in deblending sources. Furthermore, when we use the `cmodel` magnitudes to select emission-line galaxies, some candidates are found to be unnaturally clustered over small area. Therefore, we decided to use the magnitude with the small aperture on the undeblended images to measure the colors in the central 1.1 arcsec region of galaxies for the selection of emission-line galaxies.

A slight difference in effective wavelength between NB and BB filters requires us to correct for the color term to properly estimate the stellar continuum underlying an emission line. In Hayashi et al. (2018), we used the stellar population synthesis models to estimate the intrinsic col-

Table 4. Filters used for the selection of emission-line galaxies.

NB	BBs	weights	mag cut	color cut	EW _{obs}
NB527	g, r	0.674, 0.326	>18.5	>0.25	22Å
NB718	r, i	0.079, 0.921	>18.5	>0.25	32Å
NB816	i, z	0.631, 0.369	>18.5	>0.25	33Å
NB921	z, y	0.643, 0.357	>18.5	>0.20	35Å
NB973	z, y	0.052, 0.948	>18.5	>0.20	27Å

ors of the stellar continuum for galaxies at redshifts that the NB filters can probe, and then correct for the color terms using the average relation between the intrinsic BB-NB and the observed BB colors in each redshift. This time, we linearly interpolate to estimate the continuum flux density at the NB wavelength by taking a weighted average of two BB magnitudes (see also Appendix of Vilella-Rojo et al. 2015). Note that the weights are tuned so that the galaxies without emission lines at the wavelength of NB filter distribute around the sequence of $BB_{\text{corrected}} - NB = 0$ with photometric errors. The weights used are shown in table 4. Figure 6 shows the color–magnitude diagram of BB-NB versus NB.

Then, we select galaxies showing more than 5σ excess against the photometric error in BB-NB color as candidates of emission-line galaxies. Note that we estimate the photometric error for the individual objects and thus a single curve of the selection criterion, which is often seen in studies of NB-selected emission-line galaxies, cannot be drawn in figure 6. We also apply a BB-NB color cut to remove the bright galaxies with intrinsic red colors in the stellar continuum. The values of the color cut are smaller than those of PDR1, which allows us to select emission-line galaxies with lower EW of emission line. The limiting observed EWs are 22, 32, 33, 35, and 27 Å for NB527, NB718, NB816, NB921, and NB973, respectively. We also apply a magnitude cut of >18.5 mag to conservatively remove too bright objects that may be saturated in HSC images. We set the magnitude based on the color–magnitude diagram of BB-NB versus NB used for the selection of emission-line galaxies (figure 6). Setting the magnitude cut can cause us to miss emission-line galaxies at the very bright end (Drake et al. 2013; Stroe et al. 2014; Hayashi et al. 2018). Since the cut of 18.5 mag is one magnitude fainter than that in the PDR1, we must take care of the magnitude cut to discuss the bright end of luminosity functions in this study.

Some emission-line galaxies with significant color excess near the selection criterion can be missed due to the photometric errors. To estimate the completeness of the selection, we add a photometric error in each band randomly from a normal distribution with 1σ sky noise and apply the selection criteria to the magnitudes. We try 1000 iterations

⁴ <https://hsc-release.mtk.nao.ac.jp/>

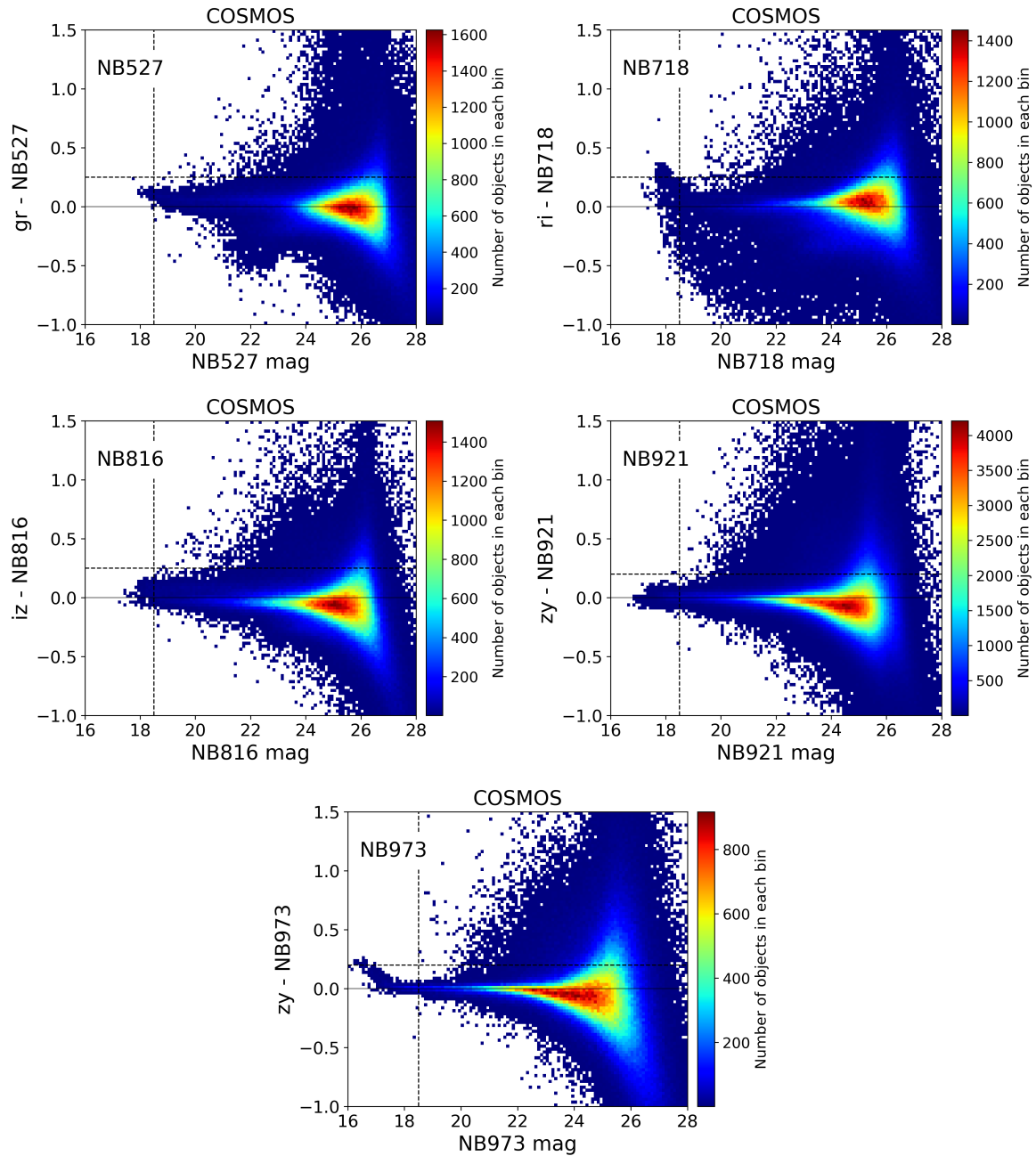


Fig. 6. The distribution of objects in the COSMOS field in the color–magnitude diagram of BB–NB versus NB, which is color-coded by the number of the objects in each bin. The BB magnitude is corrected for the color term by interpolating with two filters and weights shown in table 4. The dotted lines are the magnitude cut and color cut applied for the selection (table 4). The solid line shows the color of BB–NB= 0.

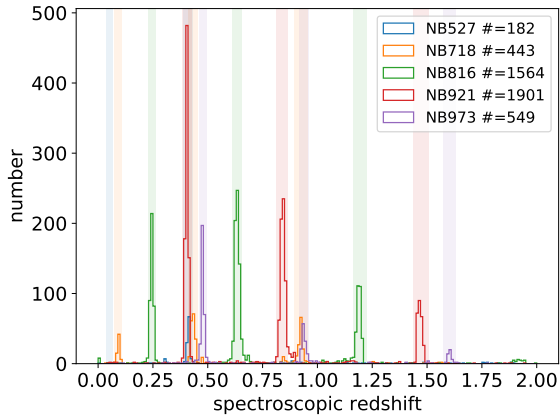


Fig. 7. The distribution of spectroscopic redshift for galaxies with color excess in BB-NB. The number of the galaxies with spectroscopic redshifts is shown in the legend. The regions with pale colors show the redshift ranges of emission-line galaxies expected by the wavelength range of each NB filter.

to see how many times the individual emission-line galaxies meet the criteria and then estimate the selection completeness. We multiply the selection completeness by the detection completeness in each bands to derive the completeness of individual emission-line galaxies. Hereafter, unless otherwise mentioned, the completeness takes account of both detection completeness and selection one. In this study, we limit the samples to galaxies with the completeness greater than 0.5.

Figure 7 shows the spectroscopic redshift distribution of emission-line galaxy candidates. The peaks of distribution are clearly seen at the expected redshifts. The redshift distribution of the galaxies with significant excess in the BB-NB color suggests the validity of our selection method as well as low contaminants among the selected galaxies.

3.2 Identification

We first use spectroscopic redshifts (§2.2) to identify the emission lines if available. If a galaxy has a spectroscopic redshift outside of the range expected from any NB filters, we remove it as a contaminant.

Next, we use photometric redshifts. In the PDR2, the photometric redshifts from two codes (DEMP and Mizuki, Tanaka et al. 2018; Nishizawa et al. 2020) are available. For the NB527, NB718, and NB973 emitters selected from CHORUS in the UD-COSMOS field, we also use the photometric redshifts from the COSMOS2015 catalog (Laigle et al. 2016). For the NB816 and NB921 emitters from HSC-SSP, we use only the photometric redshifts calculated with HSC five BBs to keep the consistency among the D/UD fields. We rely on the photometric redshifts with $\Delta z_{phot}/(1.0 + z_{phot}) \leq 0.2$, where Δz_{phot} is a 68%

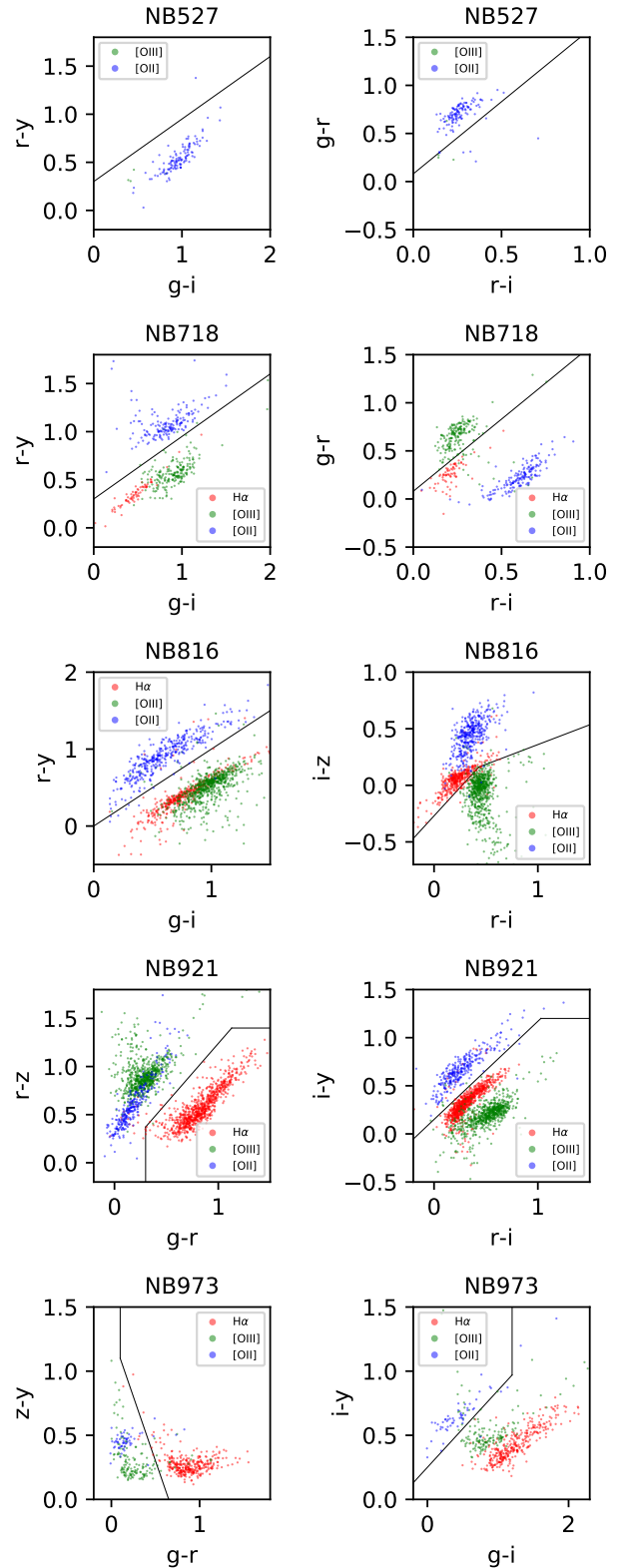


Fig. 8. Two color diagrams to identify emission line galaxies based on the colors of galaxies. The galaxies with spectroscopic redshifts are plotted and color-coded based on the redshifts. Note that the color selection is applied for emission-line galaxies for which the spectroscopic redshift is not available and photometric redshifts are not well determined.

confidence interval. When the redshift range estimated from the width of NB filter is overlapped with the 68% confidence interval, the redshift is assigned to the galaxy. In the case that all of the photometric redshifts available are consistent in each galaxy, the emission-line galaxies are identified based on the photometric redshift.

Finally, for galaxies not identified with spectroscopic or photometric redshifts, we use colors to identify the emission lines. Figure 8 shows the color-color diagrams to distinguish the emission-line from the other possibilities. The color criteria are determined based on the colors for emission-line galaxies with spectroscopic redshifts: In NB527, for [OII]

$$g - r > 1.50(r - i) + 0.08$$

otherwise, [OIII] emitters. In NB718, first one is for [OII] and the second is for [OIII]

$$r - y > 0.65(g - i) + 0.30,$$

$$g - r > 1.50(r - i) + 0.08,$$

otherwise, H α . In NB816, for [OII], H α ,

$$r - y > g - i,$$

$$i - z > (r - i) - 0.27 \vee i - z > 0.35(r - i) + 0.01,$$

otherwise, [OIII]. In NB921, for H α , [OII],

$$r - z \leq 1.4 \wedge g - r \geq 0.3 \wedge r - z \leq 1.24(g - r),$$

$$i - y > 1.2 \vee i - y > 1.02(r - i) + 0.15,$$

otherwise, [OIII]. In NB973, for H α , [OII],

$$g - r \geq 0.1 \wedge z - y > 2.0(g - r) + 1.30,$$

$$g - i \leq 1.2 \wedge i - y > 0.6(g - i) + 0.25,$$

otherwise, [OIII].

There is H β emission line near [OIII]. We remove H β emission-line galaxies based on the spectroscopic and photometric redshifts (see also Hayashi et al. 2018). It is impossible to distinguish H β from [OIII] based on the color-color diagrams. Therefore, some of [OIII] emission-line galaxies identified by the colors can be a contaminant of H β emission-line galaxy. However, figures 5 and 7 show that contamination of H β emission-line galaxies in the sample of [OIII] emission-line galaxies is small (see also Sobral et al. 2015; Khostovan et al. 2016). There are [NII] doublet lines close to H α line, which implies that all of the emission lines can enter the NB filter simultaneously. Although [NII] lines are weaker than or comparable to H α at most (e.g., Baldwin et al. 1981), we discuss the contribution of [NII] lines to the measurement of H α emission-line flux in section 4.

To summarize, we identify 75,377 emission-line galaxies

with completeness more than 0.5 using NB816 and NB921 from the HSC-SSP and NB527, NB718, and NB973 from the CHORUS. The numbers of each population are listed in table 5.

3.3 Contamination

We succeed in reducing the contamination rate compared to that in the PDR1 catalog. This is within expectations that figure 7 demonstrates. As with the PDR1 emitter catalogs, we investigate the contamination rate by applying the photo- z and color selections to galaxies confirmed with spectroscopic redshifts. Note that here we do not use the spectroscopic redshifts obtained by the follow-up spectroscopy (§ 2.2.2–2.2.3) for NB emitter candidates selected from the HSC-SSP PDR1 data. That is, we use the only spectroscopic redshifts (§ 2.2.1) for the targets unbiased towards the NB emitters to estimate the contamination rate.

Among the galaxies with spec- z that meet the photo- z or color selection, more than 90% of the galaxies have the spectroscopic redshifts expected from the wavelength of the NB filter, except for NB921 [OII] emitters and NB718 H α emitters. The NB921 [OII] emitters that meets the criteria is 81.5%, while that for the NB718 H α emitters is 84.2%. As a result, we estimate the contamination rate to be less than 10% for most cases and $\sim 20\%$ at most, which suggests that the contamination rate of the emitter catalogs from the PDR2 is much improved compared with the PDR1 catalogs (13–43%, Hayashi et al. 2018).

3.4 Emission-line galaxies with an AGN

In the PDR1 catalog, a small fraction of emission-line galaxies ($\sim 0.1\%$) have counterparts in the X-ray. However, we were not able to fully reject the possibility that excluding point sources from the PDR1 catalog results in the small fraction of the X-ray sources in the emitter sample. Since we do not exclude point sources explicitly to avoid the possible selection bias in the PDR2 catalogs, we revisit the X-ray counterparts in the emission-line galaxies selected by the PDR2 data by using the catalog of 4016 X-ray sources selected from the 4.6Ms X-ray data by the Chandra COSMOS Legacy Survey (Marchesi et al. 2016; Civano et al. 2016). Additionally, we find counterparts in a catalog of 2937 radio-selected AGNs from the VLA-COSMOS 3 GHz Large Project (Delvecchio et al. 2017).

We use 3534 X-ray sources that have an optical/IR counterpart located in the UD-COSMOS field. Then, we match 14,754 emission-line galaxies in the UD-COSMOS

Table 5. Summary of the emission-line galaxies with completeness more than 0.5.

line	filter	redshift	number	field			
				SXDS+XMM-LSS	COSMOS	ELAIS-N1	DEEP2-3
[OIII]	NB527	0.050	130	–	130	–	–
H α	NB718	0.092	331	–	331	–	–
H α	NB816	0.246	5400	1053	436	2603	1308
H α	NB921	0.404	8532	571	2554	2479	2928
[OII]	NB527	0.411	729	–	729	–	–
[OIII]	NB718	0.432	1075	–	1075	–	–
H α	NB973	0.479	919	–	919	–	–
[OIII]	NB816	0.633	10323	2910	748	3823	2842
[OIII]	NB921	0.840	14647	1678	6376	2872	3721
[OII]	NB718	0.923	1238	–	1238	–	–
[OIII]	NB973	0.939	1211	–	1211	–	–
[OII]	NB816	1.193	15301	3885	1666	5579	4171
[OII]	NB921	1.471	14586	2460	4878	4512	2736
[OII]	NB973	1.605	955	–	955	–	–

field with a completeness larger than 0.5 to the X-ray sources. As a results, 66 emission-line galaxies have an X-ray counterpart ($\sim 0.45\%$). Although the fraction is slightly larger than that from the PDR1 catalog, the fraction of emission-line galaxies detected in the X-rays is undoubtedly small. Among 66 X-ray sources, 13 sources are H α emitters, 20 sources are [OIII] emitters, and 33 sources are [OII] emitters. Next, 2639 radio-selected AGNs in the UD-COSMOS field are matched with the emission-line galaxies. After removing the 21 radio sources that are also matched X-ray sources, there remains 30 emission-line galaxies found as a radio-selected AGN. Among them, 3 sources are H α emitters, 11 sources are [OIII] emitters, and 16 sources are [OII] emitters. As a result, about 0.65% of the emission-line galaxies have an AGN selected in X-ray and/or radio. As shown in table 3, the [OII] emitters tend to be at higher redshifts, and thus the luminosities of emission-line are likely larger than those of H α emitters at lower redshifts. Although some emitters have the luminosity of emission line larger than L^* derived in § 4, many emitters have the luminosity lower than L^* . Therefore, the emission-line galaxies with the X-ray/radio counterpart do not necessarily dominate the bright end of luminosity function.

As shown in figure 5, our follow-up spectroscopy succeeds in detecting multiple emission lines from the emitters. We note that the AAT/AAOmega spectroscopic data can be used to investigate further the fraction of AGN in the H α emitters at $z = 0.246$ and 0.404 based on the BPT diagram with H β , [OIII], H α , and [NII] emission lines (Baldwin et al. 1981). We will address this in the forthcoming paper.

3.5 Stellar mass

As with the PDR1 catalog (Hayashi et al. 2018), stellar mass for the emission-line galaxies is calculated by spectral energy distribution (SED) fit with five HSC BB data at the fixed redshift using the code with Bayesian priors (Mizuki: Tanaka 2015). If available, the redshift is fixed to a spectroscopic redshift, otherwise, the redshift is assumed to that estimated from the central wavelength of NB. The model SED templates of galaxies are generated by the code of Bruzual & Charlot (2003), and nebular emission lines are taken into account. Solar metallicity and the extinction curve of Calzetti et al. (2000) are adopted. Readers should refer to Section 3.6 of Hayashi et al. (2018) for more details.

3.6 Spatial distribution

Figure 9 shows the spatial distributions of H α , [OIII], and [OII] emission-line galaxies in the COSMOS field. The spatial distributions of emission-line galaxies in the other fields are shown in the figures in Appendix 2. The distributions are consistent with those from the PDR1 catalogs (Hayashi et al. 2018).

Recently, several studies report the large-scale structures revealed by the large spectroscopic surveys at redshifts matched with those of our NB emitters (table 3). Paulino-Afonso et al. (2018) show a super cluster at $z = 0.84$ confirmed by VLT/VIMOS spectroscopy, whose redshift is covered by NB921 [OIII] emitters. Hasinger et al. (2018) show a redshift spike at $z = 1.458$ confirmed by Keck/DEIMOS spectroscopy, whose redshift is covered by NB921 [OII] emitters. Böhm et al. (2020) spectroscopically confirm two overdensities of NB921 [OII] emitters at $z = 1.47$ selected from the HSC-SSP PDR1 data using

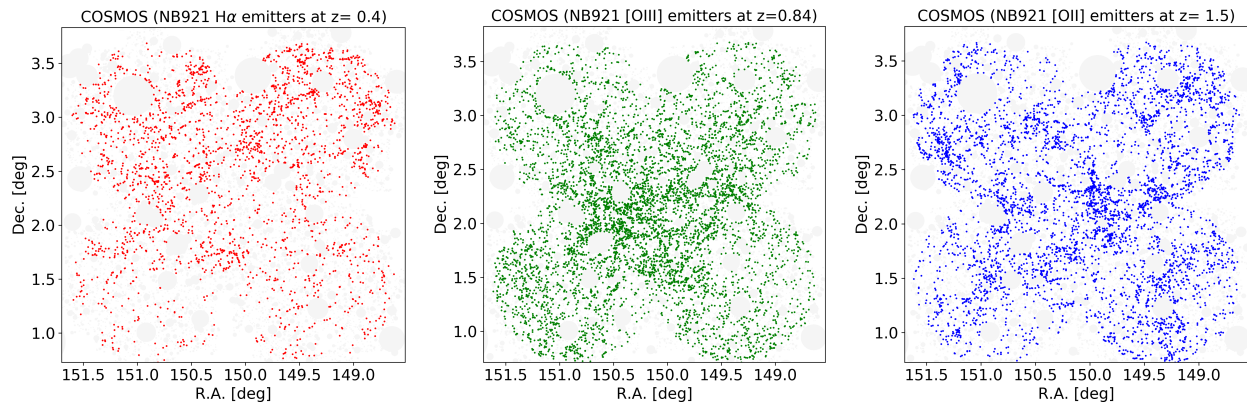


Fig. 9. The spatial distribution of NB921-selected H α , [OIII], and [OII] emission-line galaxies in the COSMOS field. The masked regions are shown in gray. The distribution of the other emission-line galaxies selected in this study is shown in Appendix 2.

VLT/KMOS. Our samples of emission-line galaxies reproduce all of the structures spectroscopically confirmed, suggesting the effectiveness of NB imaging survey to reveal the large-scale structures at specific redshifts.

4 Emission-line luminosity functions

Luminosity function is often expressed with the form of a Schechter function (Schechter 1976):

$$\phi(L)dL = \phi^* \left(\frac{L}{L^*}\right)^\alpha \exp\left(-\frac{L}{L^*}\right) d\left(\frac{L}{L^*}\right),$$

or

$$\phi'(L)d(\log L) = \phi'^* \left(\frac{L}{L^*}\right)^{\alpha+1} \exp\left(-\frac{L}{L^*}\right) \ln 10 d(\log L),$$

where L^* , ϕ^* (or ϕ'^*) and α are Schechter parameters. L^* is a characteristic luminosity, ϕ^* (or ϕ'^*) is a normalization density at L^* , and α is an exponential power of the function dominant at faint end. The normalization densities in the two forms are related by $\phi^* = \ln 10 \phi'^*$.

We derive the luminosity functions in the same way as Hayashi et al. (2018). First, we derive fluxes of the emission lines from the NB and BB photometry. The BB–NB color and the total flux density in NB are required to calculate emission-line flux using the equation (7) of Hayashi et al. (2018). We use the `undebled_convolvedflux_2_11` magnitudes for the colors and the `cmodel` magnitudes for the total flux density. Then, the fluxes are converted to luminosities using the spectroscopic redshifts if available, otherwise, redshifts estimated from the central wavelength of NB. In the following section, we compare the luminosity functions of emission-line galaxies at different redshifts and discuss the redshift evolution. As shown in table 4, the limiting observed EWs (thus rest-frame EWs as well) are different between the NB data. For a fair comparison, hereafter, we

only use the H α emission-line galaxies with a rest-frame EW larger than 29.3Å at each redshift, the [OIII] emitters with a rest-frame EW larger than 22.3Å, and the [OII] emitters with a rest-frame EW larger than 16.6Å.

For H α emitters, not only H α emission line but also [NII] doublet enter the NB filter simultaneously due to small separation in wavelength between the lines. We estimate the contribution of [NII] line to the fluxes measured with NB and BB photometry, based on the line flux ratio of the local galaxies with a given stellar mass and line luminosity (see Appendix 2 of Hayashi et al. 2018). The sample of the local galaxies are selected from the SDSS so that the galaxies have equivalent widths of emission lines similar to the NB emission-line galaxies selected in this study. The other line ratios (i.e., H α /H β) for the local galaxies are used later as well for correction for dust attenuation. We notice that we should check whether the line ratios of the local galaxies are valid for the emission-line galaxies at higher redshifts up to $z \sim 1.6$. We will investigate the line ratios of the emission-line galaxies using the spectra taken by our follow-up observations (§ 2.2.2–2.2.3) in the forthcoming paper. In this paper, we assume that the emission-line galaxies selected in this study follow the same relations in the line ratios as the local SDSS galaxies.

Since the transmission curve of HSC NB filters is not a perfect top-hat (Figure 1), the survey volume for individual emission line galaxies is dependent on the luminosities. Because only emission lines with fluxes observed above a limiting flux can be detected, galaxies with an intrinsically larger flux can be selected even at wavelengths with lower transmission, which means that intrinsically brighter emission-line galaxies can be selected over a wider range of redshifts than fainter emission-line galaxies. For a given luminosity, the minimum and maximum redshifts where the emission line can be observed at more than 5 σ are calcu-

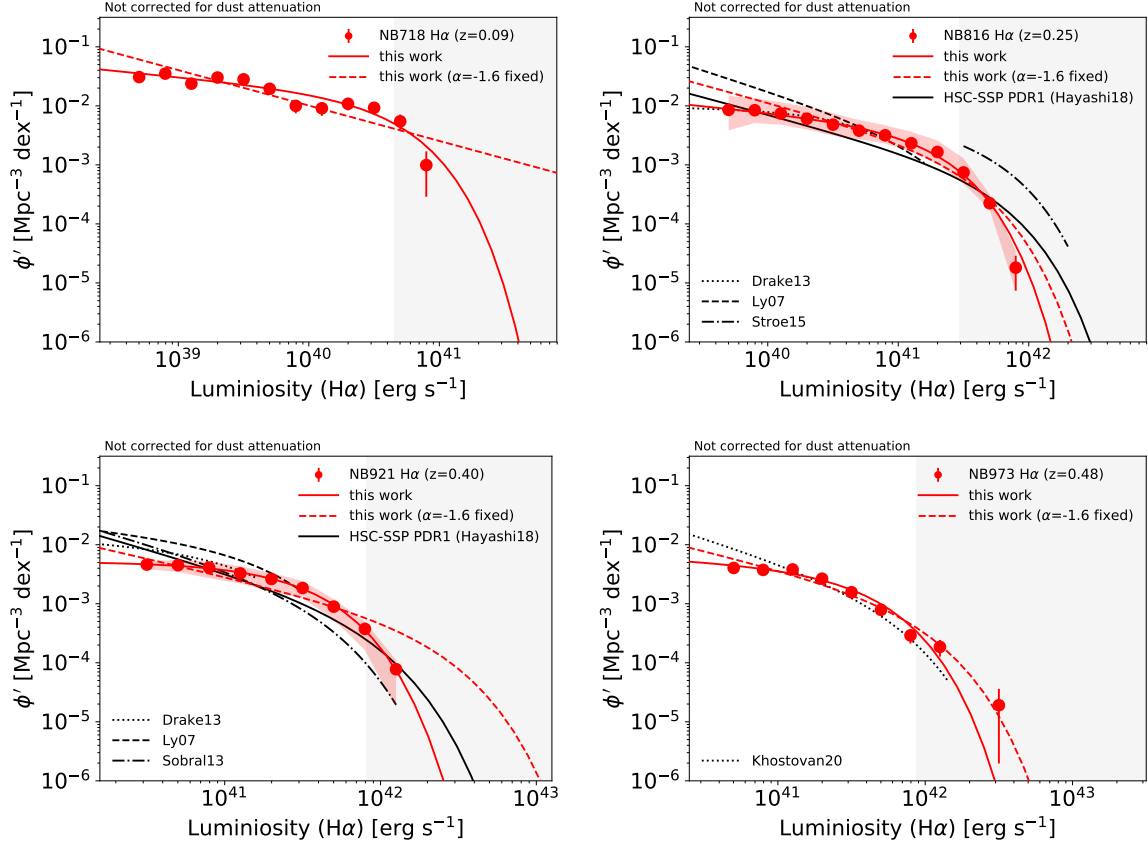


Fig. 10. The luminosity functions of H α emission-line galaxies. The filled circles show the measurement with equation (2) and the error bars show the Poisson error. The pale red region shows the variation in the four discrete areas of HSC-SSP D/UD layer. Note that since the NB527, NB718, and NB973 data from the CHORUS survey are available in the UD-COSMOS field only, the pale region cannot be drawn for the luminosity functions of the emitters selected from the three NB data. The red line is a Schechter function fitted to the measurement with free parameters of L^* , ϕ'^* and α . The dashed line is also a Schechter function fitted with α fixed to be -1.6 . The black line is the result from HSC-SSP PDR1 by Hayashi et al. (2018). The black dotted line, dashed line, and dash-dotted line are the luminosity functions from the literature (Ly et al. 2007; Drake et al. 2013; Sobral et al. 2013; Stroe & Sobral 2015; Khostovan et al. 2020), where the luminosity range covering the data in each study is shown. The gray area shows the luminosity range where the completeness could be lower than what we estimate because of the magnitude cut of 18.5 mag.

Table 6. Parameters of the Schechter function fitted to the luminosity function.

line	redshift	NB	No correction for dust attenuation			Corrected for dust attenuation		
			$\log\left(\frac{\phi'^*}{\text{Mpc}^{-3} \text{ dex}^{-1}}\right)$	$\log\left(\frac{L^*}{\text{erg s}^{-1}}\right)$	α	$\log\left(\frac{\phi'^*}{\text{Mpc}^{-3} \text{ dex}^{-1}}\right)$	$\log\left(\frac{L^*}{\text{erg s}^{-1}}\right)$	α
O3E	0.050	NB527	-2.73 ± 0.53	40.60 ± 0.75	-1.44 ± 0.10	-2.73 ± 0.50	40.60 ± 0.71	-1.43 ± 0.09
HAE	0.092	NB718	-2.23 ± 0.19	40.66 ± 0.19	-1.22 ± 0.10	-2.48 ± 0.36	41.06 ± 0.51	-1.29 ± 0.12
HAE	0.246	NB816	-2.75 ± 0.04	41.27 ± 0.02	-1.22 ± 0.04	-3.16 ± 0.07	41.89 ± 0.07	-1.36 ± 0.03
HAE	0.404	NB921	-2.65 ± 0.02	41.47 ± 0.02	-1.00 ± 0.03	-2.91 ± 0.07	41.98 ± 0.05	-1.14 ± 0.05
O2E	0.411	NB527	-3.17 ± 0.17	41.58 ± 0.13	-1.44 ± 0.10	-3.01 ± 0.07	41.70 ± 0.06	-1.26 ± 0.04
O3E	0.432	NB718	-3.62 ± 0.28	42.04 ± 0.19	-1.80 ± 0.10	-2.91 ± 0.20	41.72 ± 0.15	-1.40 ± 0.14
HAE	0.479	NB973	-2.77 ± 0.14	41.57 ± 0.10	-1.12 ± 0.17	-3.29 ± 0.26	42.25 ± 0.20	-1.42 ± 0.17
O3E	0.633	NB816	-3.02 ± 0.20	41.70 ± 0.12	-1.34 ± 0.17	-3.14 ± 0.21	41.98 ± 0.12	-1.39 ± 0.16
O3E	0.840	NB921	-3.33 ± 0.29	42.15 ± 0.16	-1.65 ± 0.21	-3.58 ± 0.29	42.55 ± 0.17	-1.72 ± 0.17
O2E	0.923	NB718	-2.79 ± 0.16	41.66 ± 0.11	-1.11 ± 0.22	-3.14 ± 0.15	42.23 ± 0.10	-1.39 ± 0.13
O3E	0.939	NB973	-3.12 ± 0.22	42.10 ± 0.16	-1.33 ± 0.19	-3.04 ± 0.24	42.24 ± 0.18	-1.23 ± 0.24
O2E	1.193	NB816	-2.72 ± 0.17	41.84 ± 0.10	-1.30 ± 0.36	-2.86 ± 0.10	42.39 ± 0.06	-0.95 ± 0.16
O2E	1.471	NB921	-2.79 ± 0.17	42.08 ± 0.11	-1.40 ± 0.42	-3.06 ± 0.14	42.80 ± 0.09	-1.39 ± 0.25
O2E	1.605	NB973	-3.98 ± 0.92	42.79 ± 0.53	-1.98 ± 0.38	-3.10 ± 0.15	42.81 ± 0.12	-1.04 ± 0.23

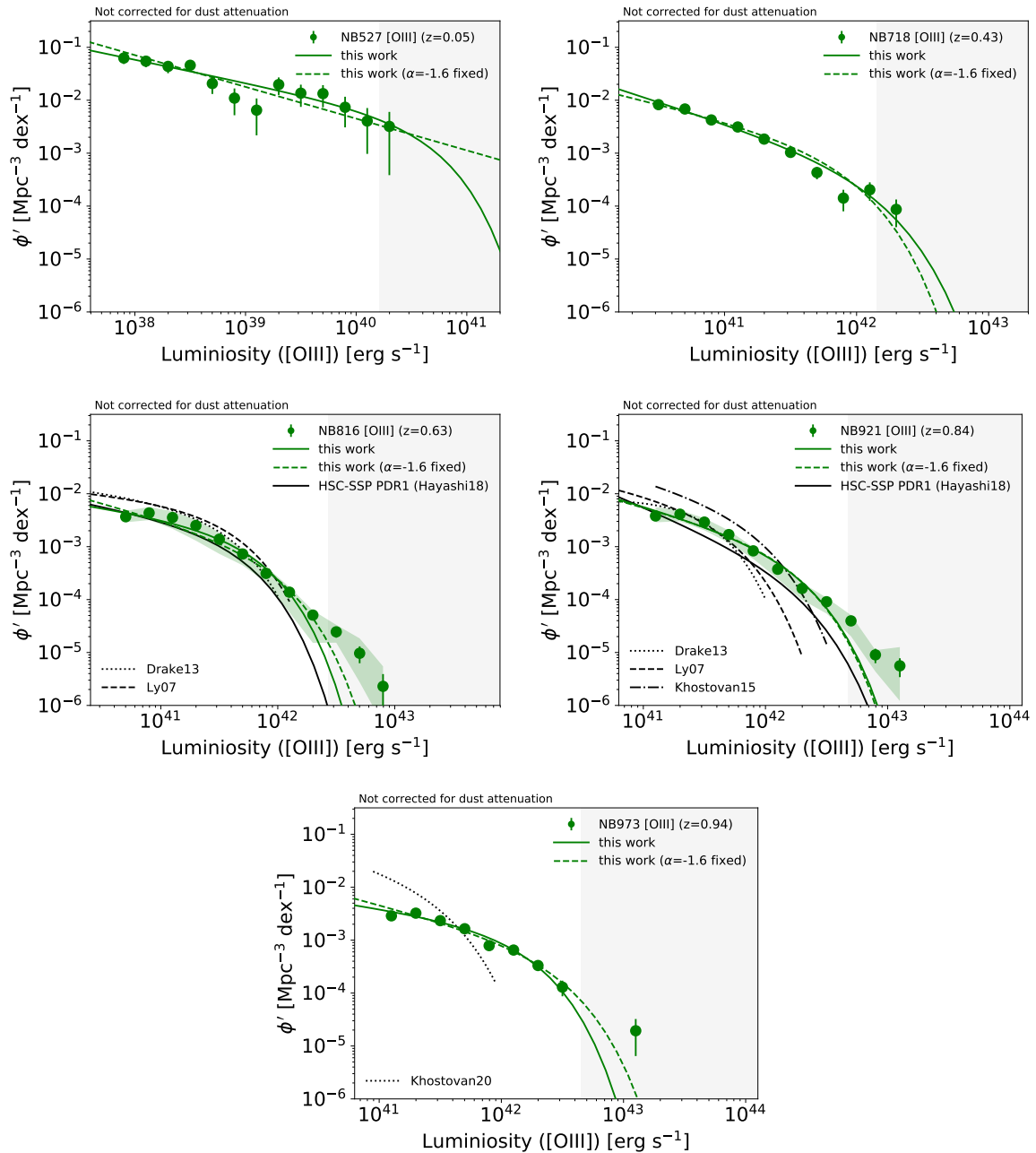


Fig. 11. The same as fig 10, but for [OIII] emission-line galaxies. The luminosity functions from the literature are also shown for comparison (Ly et al. 2007; Drake et al. 2013; Khostovan et al. 2015; Khostovan et al. 2020).

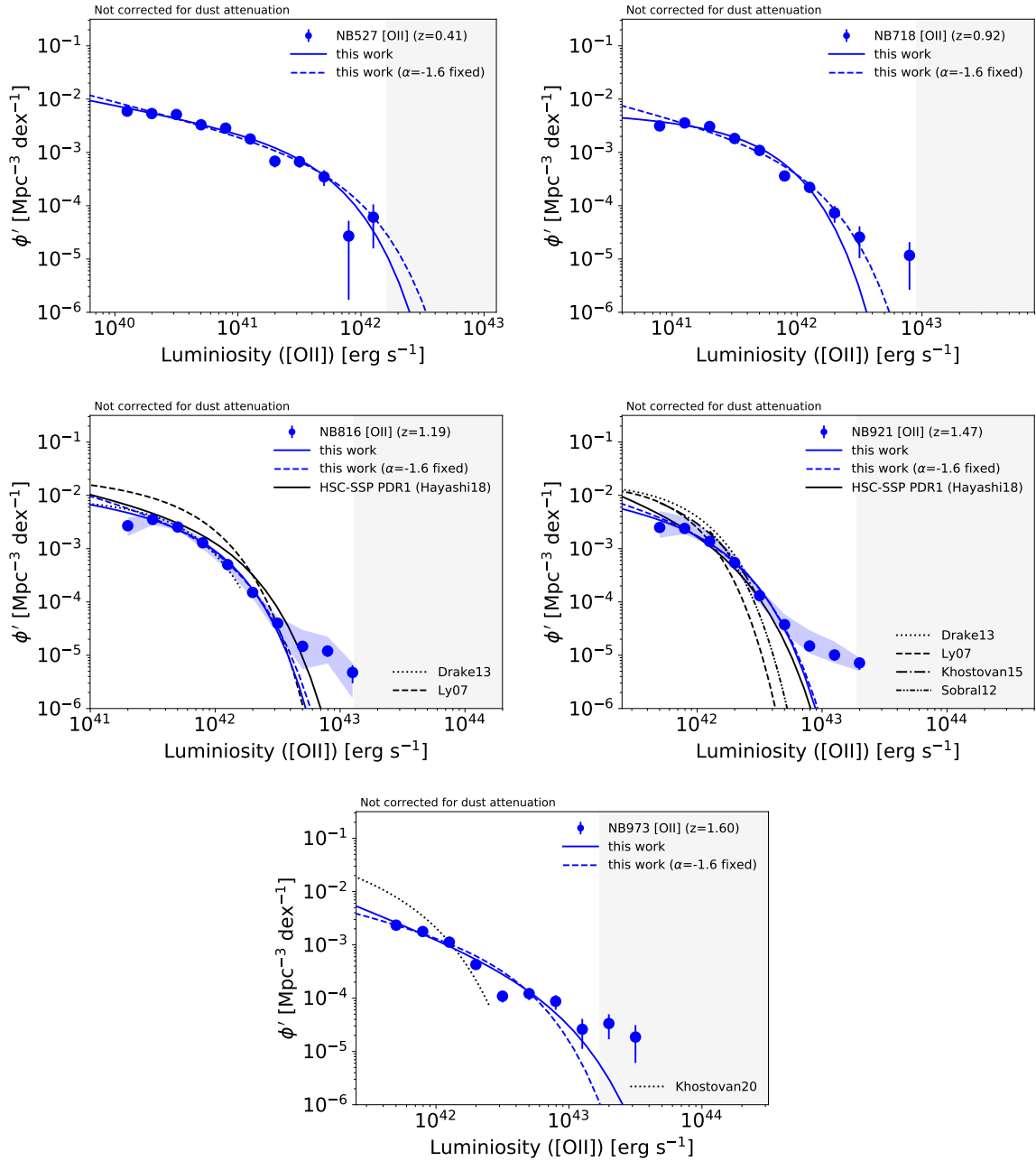


Fig. 12. The same as fig 10, but for [OII] emission-line galaxies. The luminosity functions from the literature are also shown for comparison (Ly et al. 2007; Drake et al. 2013; Sobral et al. 2012; Khostovan et al. 2015; Khostovan et al. 2020).

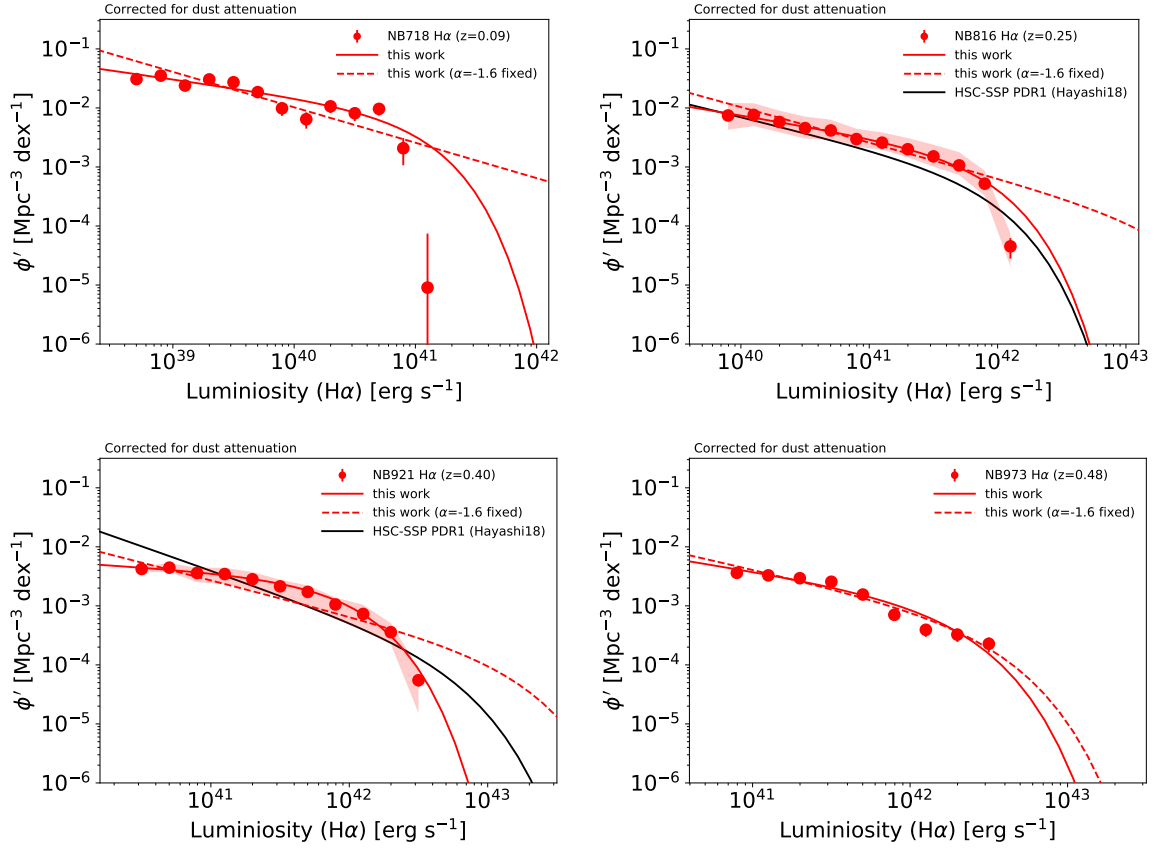


Fig. 13. The same as fig 10, but the luminosity functions are corrected for dust attenuation. See the text for the details of how to correct for the dust attenuation.

lated based on the filter transmission curve and a limiting flux. Then, the redshift range is converted to a comoving volume.

The luminosity function of emission-line galaxies is derived according to the V_{max} method:

$$\phi'_{obs}(\log L) = \sum_i \frac{1}{V_{max} \cdot f_c \cdot \Delta(\log L)}, \quad (1)$$

where i is for individual galaxies with $\log L \pm 0.5\Delta(\log L)$, V_{max} is the survey volume and f_c is completeness taking account of both selection and detection completeness. In the PDR1 catalog, we assumed that the emission line is observed at the central wavelength of the NB filter. This assumption can result in underestimating the line luminosities of galaxies at redshifts away from the filter center. In this study, we correct the luminosity function, $\phi'_{obs}(\log L)$, derived from equation (1) for an impact of filter response function to obtain intrinsic luminosity function, $\phi'(\log L)$ (see also Sobral et al. 2009; Sobral et al. 2013; Sobral et al. 2018 for correction of filter response function). Here, we assume a uniform redshift distribution within a redshift range corresponding to the wavelength range of the NB filter, because the survey area is large

enough to overcome the field-to-field variance. For individual emission-line galaxy with a given observed luminosity, the distribution of intrinsic luminosities expected within the possible redshift range can be estimated from the filter response function under the assumption of the uniform redshift distribution. Then, by combining with the observed luminosity function derived from equation (1), the probability distribution, $P_i(\log L)$, of the individual expected intrinsic luminosities is estimated for each object;

$$P_i(\log L) = \phi'_{obs}(\log L) / \int \phi'_{obs}(\log L') d(\log L').$$

By taking account of the probability distribution of the intrinsic luminosities, the luminosity function can be derived as follows;

$$\phi'(\log L) = \sum_i \frac{P_i(\log L)}{V_{max} \cdot f_c \cdot \Delta(\log L)}.$$

The correction allows us to derive the bright end of luminosity functions more properly, because there is the possibility that the observed luminosity can be underestimated due to the nonuniformity on the filter response function.

Finally, we correct the luminosities for dust attenuation to derive the intrinsic luminosity functions. To do that, we

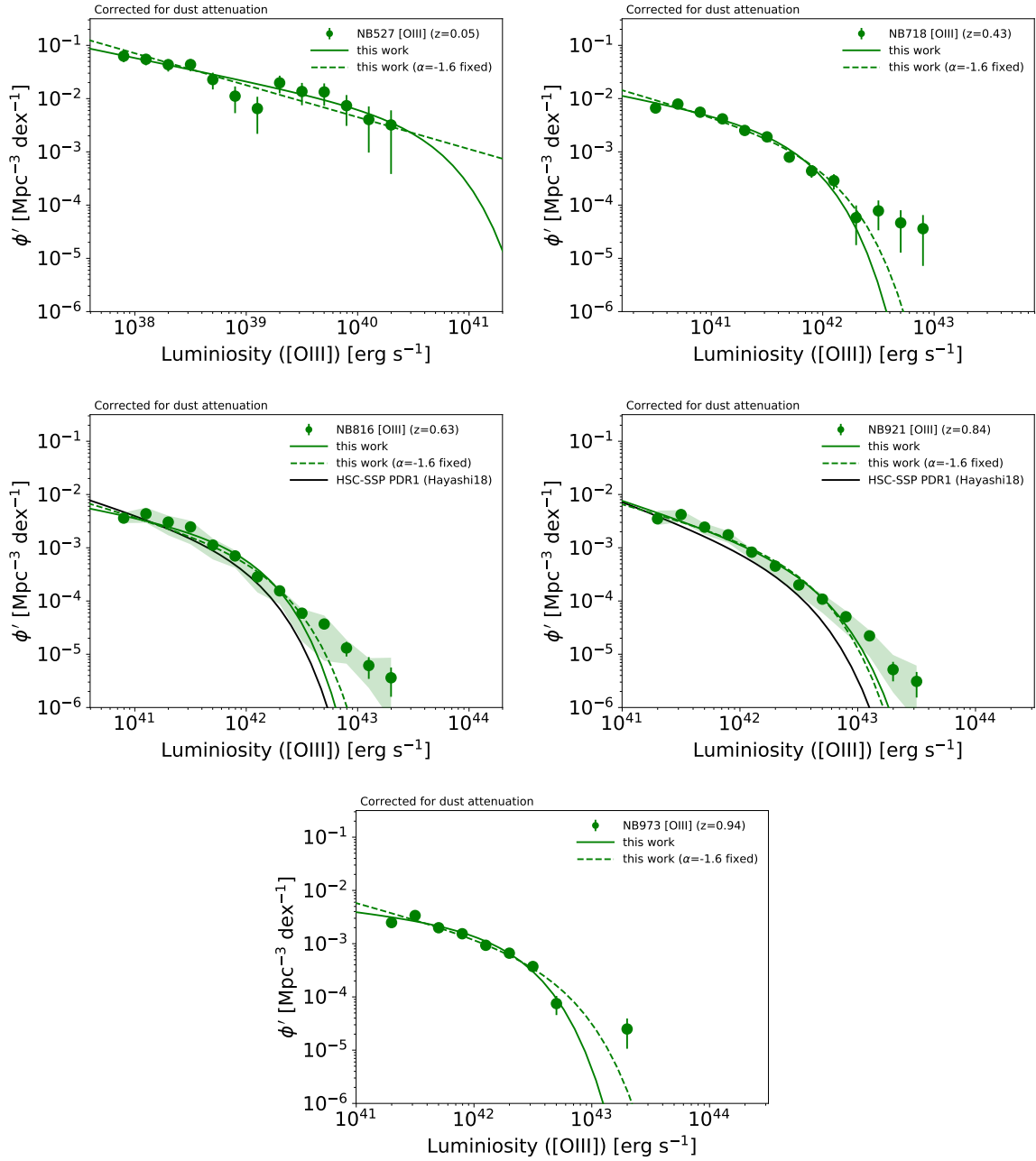


Fig. 14. The same as fig 13, but for [OIII] emission-line galaxies.

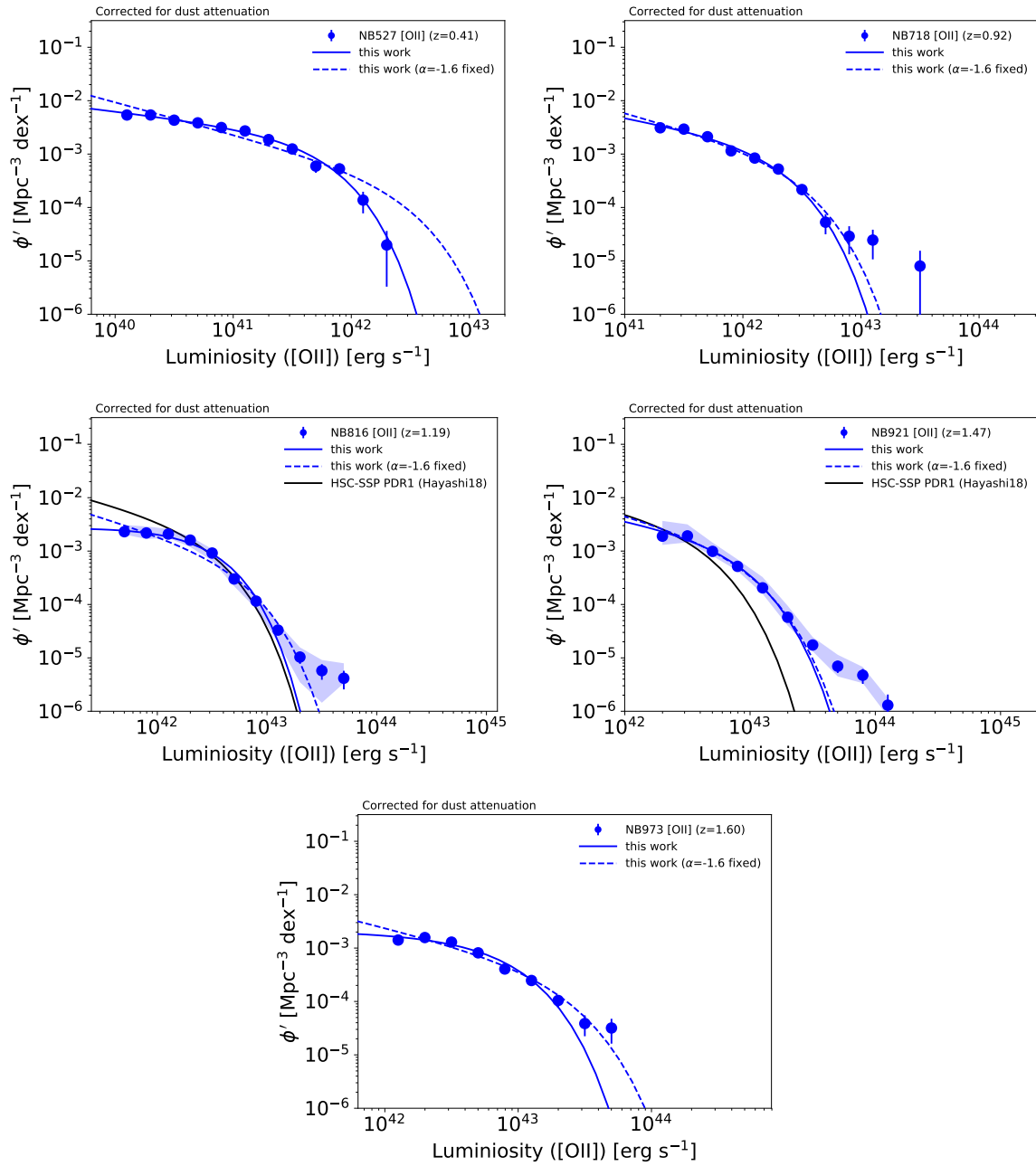


Fig. 15. The same as fig 13, but for [OII] emission-line galaxies.

use the relation between the line luminosity, stellar mass and Balmer decrement (the ratio of $H\alpha$ to β) in the SDSS sample of the emitter analogs. Note that we assume the Cardelli et al. (1989) extinction curve and the intrinsic $H\alpha/H\beta$ ratio of 2.86 for Case B recombination under an electron temperature of $T_e = 10^4$ K and electron density of $n_e = 10^2 \text{ cm}^{-3}$ (Osterbrock 1989),

Figures 10–12 show the observed luminosity functions for $H\alpha$, [OIII], and [OII] emitters at each redshift. Figures 13–15 show the dust-corrected intrinsic luminosity functions for $H\alpha$, [OIII], and [OII] emitters at each redshift. For the emission-line galaxies selected from the HSC-SSP data (i.e., NB816 and NB921), the variation of the measurements of the luminosity function in the four discrete areas of HSC-SSP D/UD layer is shown by the pale color region. While a Schechter function fitted to the measurement with free parameters of L^* , ϕ'^* and α is shown by solid line, the dashed line is a result fitted with α fixed to be -1.6 . In the fitting, we take account of the field variation as an uncertainty for the emitters selected from NB816 or NB921 data, while the Poisson error is taken into account for the other emitters. The best-fit Schechter parameters are summarized in table 6.

The luminosity functions in this study are almost consistent with our previous study with the PDR1 data (Hayashi et al. 2018) that is shown by the black solid line. Note that since we select emission-line galaxies with an EW lower than those by our previous study (§ 3), the selection of emission-line galaxies from the PDR2 data is not perfectly the same as our study with the PDR1 data as well as the other previous studies (Ly et al. 2007; Sobral et al. 2012; Drake et al. 2013; Sobral et al. 2013; Stroe & Sobral 2015; Khostovan et al. 2015; Khostovan et al. 2020). However, it would be worth comparing the results between this study and the others. As mentioned in § 3.1, the bright end of the LF in this study can be affected by the magnitude cut applied for the selection. When a galaxy has BB-NB color applied for the color cut (table 4), the NB magnitude of 18.5 corresponds to an observed line flux of 2.7, 2.1, 1.6, 1.4, and $1.0 \times 10^{-15} \text{ erg s}^{-1} \text{ cm}^{-2}$ for NB527, NB718, NB816, NB921, and NB973 emitters, respectively. This can miss a fraction of emitters with luminosities corresponding to a few of luminosity bins in the bright end of luminosity function. The gray area in figures 10–12 shows the luminosity range affected by the magnitude cut, indicating that the bright end of the LFs in the gray area can be incomplete. It is also true that number density of objects with NB magnitude brighter than 18.5 sharply decreases (figures 2 and 18). At higher redshifts, galaxies with NB magnitude of < 18.5 would be rarer. On the other hand, the correction for the filter response function allows

us to estimate more realistic bright end of the LF. Each of the effects can impact on the bright end of LF from the opposite point of view.

For the observed $H\alpha$ LFs (figure 10), the faint end slope is flatter than the PDR1 result as well as the results from the other previous studies, which makes the observed LF more consistent with the LF expected from a semi-analytic model (Ogura et al. 2020). For the observed [OIII] LFs (figure 11), the number density is larger than that of the PDR1 LF. While the point sources were excluded from the selection in the PDR1 study, we do not exclude the point sources explicitly in this study. AGNs can be included in the sample of [OIII] emitters, compared with the PDR1 sample that shows a low AGN contamination fraction. Indeed, the fraction of the emitters that have an AGN selected in X-ray and/or radio from the PDR2 data increases by a factor of ~ 6 to be $\sim 0.65\%$ (§ 3.4). Although the [OIII] luminosity function at $z = 0.63$ is consistent with the previous studies within the uncertainty, there is a discrepancy between our results and the previous studies for the [OIII] luminosity functions at $z = 0.84$ and 0.94. The difference in the bright end can affect the parameters of the fitted Schechter function. Also, note that Khostovan et al. (2015) investigate luminosity functions of $H\beta + [\text{OIII}]$. However, the fraction of $H\beta$ is likely to be small in the samples (Sobral et al. 2015; Khostovan et al. 2016; Khostovan et al. 2020). Since the contribution of $H\beta$ becomes relatively larger in fainter luminosity range (Sobral et al. 2015; Khostovan et al. 2016), the difference of the treatment of $H\beta$ can affect the slope of the faint end of luminosity function. Follow-up spectroscopy for all [OIII] emitters is required to completely distinguish $H\beta$ from [OIII]. For the observed [OII] LFs (figure 12), the LF of the NB921-selected [OII] emitters is in good agreement with the PDR1 result, while the number density of the NB816-selected [OII] emitters is lower than the PDR1 sample. As discussed in section 3.4 of Hayashi et al. (2018), the non-negligible contaminants of red galaxies are likely to be included in the PDR1 sample of NB816 [OII] emitters. The NB816 [OII] sample is more sensitive to the effect than the NB921 sample due to the relative position in wavelength between NB and nearest BB filter (Hayashi et al. 2018). The [OII] luminosity function at $z = 1.19$ is in agreement with the result of Drake et al. (2013) and the bright end of Ly et al. (2007). The number density at L^* in our [OII] luminosity function at $z = 1.47$ is consistent with the previous studies, however, there is a large variation in the number density at the luminosity range of $> L^*$. The [OII] luminosity function at $z = 1.60$ shows a large discrepancy from the previous study of Khostovan et al. (2020). Our luminosity function has a flatter faint end as well as

more prominent excess of the bright end. Compared with the fitted Schechter function, the excess of the bright end is also seen in the LFs of [OII] emitters. The wider HSC survey tends to find the rare bright galaxies, which results in the excess of the bright end in the luminosity function of [OII] as well as [OIII]. Such excess is not seen in the LFs of H α emitters. As discussed in section 3.4, some (but not all) emitters with an AGN can contribute to the excess of the bright end of the LF.

For the luminosity functions corrected for dust extinction, it is not easy to fairly compare the results in this study with those from the previous studies, because there is a difference in the correction for filter response function and dust attenuation, which can be the other factors to cause the difference between the studies.

5 Discussions

As shown in table 3, in this study, the wide range of the 14 specific redshifts are covered by H α , [OIII], and [OII] emission lines between $z = 1.6$ and $z = 0.05$. Since the luminosities of the emission lines are sensitive to SFR of galaxies, this allows us to discuss the evolution of star-formation activity of galaxies from $z = 1.6$ down to $z = 0.05$. However, because the correlation between the intensity of [OIII] and SFR is not as strong as H α and [OII] in particular at lower redshifts as mentioned below (e.g., Moustakas et al. 2006), we do not use [OIII] emission-line galaxies in this section.

5.1 Redshift evolution of luminosity functions

The intrinsic luminosity of H α emitted from HII regions is sensitive to SFR of galaxies (e.g., Kennicutt 1998; Moustakas et al. 2006). It is known that the luminosity of [OII] is also a usable indicator of SFR in galaxies not only in the local Universe but also at high redshifts, although the relation between the luminosity and SFR in [OII] emission can depend on the physical condition of the nebular gas such as metallicity and ionization state and thus is more complicated rather than H α (e.g., Kennicutt 1998; Kewley et al. 2004; Moustakas et al. 2006; Hayashi et al. 2013; Hayashi et al. 2015). Therefore, the evolution of the luminosity functions of H α and [OII] emission-line galaxies reflects how the star-formation activities of galaxies have changed with time.

Figure 16 shows the comparison between the individual luminosity functions, where H α and [OII] lines are shown in red and blue, respectively, and the luminosity functions based on each NB data are shown with the same style. The luminosity function of emission-line galaxies at higher redshifts is likely to have larger L^* . Most of the luminosity

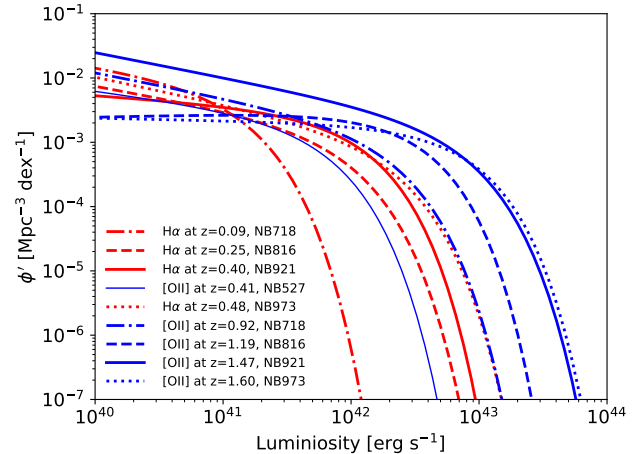


Fig. 16. The evolution of the dust-corrected luminosity functions of H α and [OII] emission-line galaxies. The Schechter functions fitted to the measurements are shown for H α in red and [OII] in blue. The luminosity functions from NB527, NB718, NB816, NB921, and NB973 are shown by thin solid line, dash-dotted line, dashed line, thick solid line, and dotted line, respectively.

function seem to have similar slope, α , of faint end. This is consistent with the well-known picture that galaxies have star formation activities peaking at $z \sim 2$, often called the cosmic noon, and then the activities gradually decrease towards the present day (e.g., Madau & Dickinson 2014).

In the next section, to further discuss the evolution of star-formation activities at $z \lesssim 1.6$ more quantitatively, we investigate the cosmic star formation rate densities.

5.2 Cosmic star formation rate densities at $z < 1.6$

To derive the star formation rate density (ρ_{SFR}), we estimate the luminosity density (ρ_L) from the dust-corrected luminosity function by integrating $L \cdot \phi(L)dL$ down to a luminosity of L . The integral is expressed with the upper incomplete gamma function:

$$\begin{aligned} \rho_L &= \int_L^\infty L' \phi(L') dL' \\ &= \int_{L/L^*}^\infty L' \phi^* \left(\frac{L'}{L^*} \right)^\alpha \exp\left(-\frac{L'}{L^*}\right) d\left(\frac{L'}{L^*}\right) \\ &= L^* \phi^* \int_{L/L^*}^\infty \left(\frac{L'}{L^*} \right)^{\alpha+1} \exp\left(-\frac{L'}{L^*}\right) d\left(\frac{L'}{L^*}\right) \\ &= L^* \phi^* \Gamma(\alpha+2, L/L^*) \end{aligned}$$

(or $= L^* \ln 10 \phi'^* \Gamma(\alpha+2, L/L^*)$).

Here, we integrate the function down to $L/L^* = 0.03$, which is the same lower limit of the luminosity as the previous studies compiled by Madau & Dickinson (2014). Then, the luminosity densities derived from H α and [OII] lines are converted to the SFR densities using the relations given by

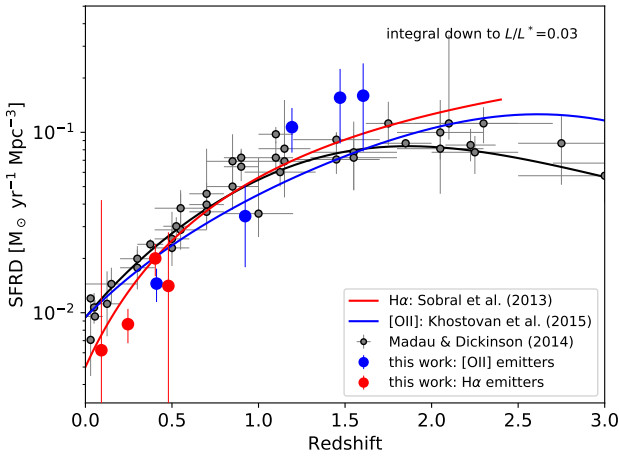


Fig. 17. The cosmic star formation rate density. The SFR densities estimated from $H\alpha$ are shown in red, and those from $[OII]$ are shown in blue. To estimate the SFR densities, the dust-corrected luminosity functions are integrated down to $L/L^* = 0.03$, and then the luminosity densities are converted to the SFR densities using the relations given by Kennicutt (1998). The gray points are the results of the previous studies (Wyder et al. 2005; Schiminovich et al. 2005; Robotham & Driver 2011; Cucciati et al. 2012; Dahlen et al. 2007; Reddy & Steidel 2009; Sanders et al. 2003; Takeuchi et al. 2003; Magnelli et al. 2011; Magnelli et al. 2013; Gruppioni et al. 2013), which are compiled by Madau & Dickinson (2014). The red and blue curves are the cosmic star-formation histories derived from $H\alpha$ and $[OII]$ SFR, respectively (Sobral et al. 2013; Khostovan et al. 2015).

Kennicutt (1998). Note that we rescale the SFR densities to those with the Chabrier (2003) IMF.

Figure 17 shows the SFR density as a function of redshift. Our results are consistent with the previous studies. Each data point is from the compilation by Madau & Dickinson 2014 and the black curve is the cosmic star-formation history fitted to the SFRDs derived from UV+IR SFR. In the comparison, the same IMF (Chabrier 2003) is assumed and the luminosity functions are integrated down to $L/L^* = 0.03$. At $z \sim 0.4$, the SFR densities can be derived from both $H\alpha$ and $[OII]$ lines, and the measurements from two lines are consistent with each other within the uncertainty. The SFR densities estimated from $H\alpha$ emitters at $z = 0.092$ and 0.479 and $[OII]$ emitters at $z = 0.411$ and 0.923 are lower than the previous studies. The emitters are selected with NB527, NB718 and NB973 data from the CHORUS survey that are available only in the UD-COSMOS field of 1.37 deg^2 . This may suggest that the survey volume for the galaxies is not sufficient to overcome the cosmic variance. Also, as shown in figure 10, our luminosity functions of $H\alpha$ emitters tend to have a flatter faint end than the previous studies, which can result in the lower luminosity (i.e., SFR) density. We note that we use the criterion of $> 5\sigma$ color excess for the selection of emission-line galaxies, while most previous

studies apply the 3σ color excess. Although we correct the luminosity function for the detection and selection completeness, our conservative criterion can make a faint end slope flatter. Furthermore, since it becomes more difficult to select emission-line galaxies with a lower EW at lower redshifts, the selection completeness of the emission-line galaxies with an EW around the limit can be lower and thus we may miss a fraction of the emission line galaxies with a smaller EW at lower redshifts. However, note that we apply the same EW cut to the emission-line galaxies used in the discussion for a fair comparison.

Several other studies on the NB-selected emission-line galaxies also study the cosmic SFR density (e.g., Ly et al. 2011; Sobral et al. 2013; Khostovan et al. 2015; Ramón-Pérez et al. 2019a; Khostovan et al. 2020; Harish et al. 2020). The red and blue curves are the cosmic star-formation histories fitted to the SFRDs derived from $H\alpha$ SFR and $[OII]$ SFR (Sobral et al. 2013; Khostovan et al. 2015), where the luminosity functions are integrated down to $L/L^* = 0$. All of the previous studies reach a consistent conclusion that the SFR densities gradually increase from the local Universe toward the redshift ~ 2 . On the other hand, the SFR densities estimated from $H\alpha$ line at $z \lesssim 0.6$ seem to be slightly lower than those for the other SFR indicators such as UV or IR (Sobral et al. 2013; Khostovan et al. 2020; Harish et al. 2020). The systematic difference is seen in our measurements as well, especially in lower redshifts. Since the NB imaging can survey only the small redshift range, the larger coverage is essential to overcome the field-to-field variance with enough survey volume. Even though the recent imaging surveys have covered larger and larger area, it is still only a few square degrees at the most in many cases. The cosmic variance can be a formidable factor even for survey covering a few square degrees. Since our $H\alpha$ emitters at $z \sim 0.246$ and 0.404 are surveyed over $\sim 16 \text{ deg}^2$, the impact of the cosmic variance would be relatively small. Nevertheless, the comparison with the cosmic SFR density (Madau & Dickinson 2014) suggests that other factors such as SFR indicators (i.e., time-scale of SF) and dust correction can also influence the measurement of the cosmic SFR density. To avoid the factors causing the possible systematic differences in the measurements, a comprehensive survey with large enough volume ($\gtrsim 5 \times 10^5 \text{ Mpc}^3$) at a wide range of redshifts would be required.

6 Conclusions

We update the catalogs of emission-line galaxies at $z \lesssim 1.6$ selected with narrowband imaging data taken with Hyper Suprime-Cam (HSC) on the Subaru Telescope. The

NB816 and NB921 data are from the second Public Data Release (PDR2) of Subaru Strategic Program (SSP) of HSC, and the NB527, NB718, and NB973 data are from the Subaru open-use intensive program, Cosmic HydrOgen Reionization Unveiled with Subaru (CHORUS) survey. The data from the HSC-SSP are available over the effective area of $\sim 16 \text{ deg}^2$ in the Deep and UltraDeep layer, while the data from the CHORUS survey are available over 1.37 deg^2 of the COSMOS field in the UltraDeep layer.

We use the data from the five NB filters to select $H\alpha$, [OIII], and [OII] emission-line galaxies at 14 specific redshifts ranging from $z \sim 1.6$ down to $z \sim 0.05$. Furthermore, 2,019 emission-line galaxies selected with the HSC-SSP PDR1 data are confirmed by our follow-up spectroscopic observations. These newly available data allow us to improve the catalogs of the emission-line galaxies. We find that compared with the PDR1 catalogs, the emission-line galaxies with lower equivalent width are selected and there is a smaller fraction of contaminants. As with our PDR1 catalogs, the PDR2 catalogs of the emitters will be published in the HSC-SSP Public Data Release website⁴

Using the catalogs of emission-line galaxies selected at small redshift intervals (i.e., the redshifts surveyed by the five NB filters are separated by $\Delta z \sim 0.2$), we show the redshift evolution of luminosity function for the emission-line galaxies. The characteristic luminosity increases for emission-line galaxies at higher redshifts, suggesting that the luminosities of emission lines at each redshift follow the cosmic star formation rate density (SFRD). By integrating the luminosity functions and then converting the luminosities of $H\alpha$ and [OII] emission lines to the star formation rates, we discuss the SFRD. The cosmic SFRD increases monotonically from the local Universe towards $z \sim 1.6$, which are consistent with the previous studies. All of the results shown in this paper demonstrate that the catalogs of emission-line galaxies at various redshifts are useful to investigate the evolution of the star-forming galaxies at $z \lesssim 1.6$. Follow-up observations, e.g., optical and/or near infrared spectroscopy and radio observation, will be the next step to study evolution of physical condition and gas content in individual star-forming galaxies since the cosmic noon.

Acknowledgments

We thank the anonymous referee for providing constructive comments and suggestions. We are grateful to Prof. Chris Lidman and Dr. Anais Möller for the instruction and support in the observations at AAT. RS acknowledges the financial support of KAKENHI (19K14766) Grant-in-Aid for Early-Career Scientists through the Japan Society for the Promotion of Science (JSPS).

This work is based on data collected at the Subaru Telescope and retrieved from the HSC data archive system, which is operated by Subaru Telescope and Astronomy Data Center (ADC) at NAOJ. Data analysis was in part carried out with the cooperation of Center for Computational Astrophysics (CfCA), NAOJ. The NB718 and NB816 filters were supported by Ehime University and the NB527, NB921 and NB973 filters were supported by KAKENHI (24244018 and 23244025) Grant-in-Aid for Scientific Research (A) through the JSPS. This work is based in part on data acquired at the Anglo-Australian Telescope, under program A/2018B/01. We acknowledge the traditional owners of the land on which the AAT stands, the Gamilaraay people, and pay our respects to elders past and present.

The Hyper Suprime-Cam (HSC) collaboration includes the astronomical communities of Japan and Taiwan, and Princeton University. The HSC instrumentation and software were developed by the National Astronomical Observatory of Japan (NAOJ), the Kavli Institute for the Physics and Mathematics of the Universe (Kavli IPMU), the University of Tokyo, the High Energy Accelerator Research Organization (KEK), the Academia Sinica Institute for Astronomy and Astrophysics in Taiwan (ASIAA), and Princeton University. Funding was contributed by the FIRST program from the Japanese Cabinet Office, the Ministry of Education, Culture, Sports, Science and Technology (MEXT), the Japan Society for the Promotion of Science (JSPS), Japan Science and Technology Agency (JST), the Toray Science Foundation, NAOJ, Kavli IPMU, KEK, ASIAA, and Princeton University.

This paper makes use of software developed for the Large Synoptic Survey Telescope. We thank the LSST Project for making their code available as free software at <http://dm.lsst.org>.

The Pan-STARRS1 Surveys (PS1) and the PS1 public science archive have been made possible through contributions by the Institute for Astronomy, the University of Hawaii, the Pan-STARRS Project Office, the Max Planck Society and its participating institutes, the Max Planck Institute for Astronomy, Heidelberg, and the Max Planck Institute for Extraterrestrial Physics, Garching, The Johns Hopkins University, Durham University, the University of Edinburgh, the Queens University Belfast, the Harvard-Smithsonian Center for Astrophysics, the Las Cumbres Observatory Global Telescope Network Incorporated, the National Central University of Taiwan, the Space Telescope Science Institute, the National Aeronautics and Space Administration under grant No. NNX08AR22G issued through the Planetary Science Division of the NASA Science Mission Directorate, the National Science Foundation grant No. AST-1238877, the University of Maryland, Eotvos Lorand University (ELTE), the Los Alamos National Laboratory, and the Gordon and Betty Moore Foundation.

Appendix 1 Validation of CHORUS NB data

We investigate the number counts, the detection completeness, and the 5σ limiting magnitude in the three NB filters from the CHORUS survey in the same manner as for the SSP data. The results are shown in figures 18–20.

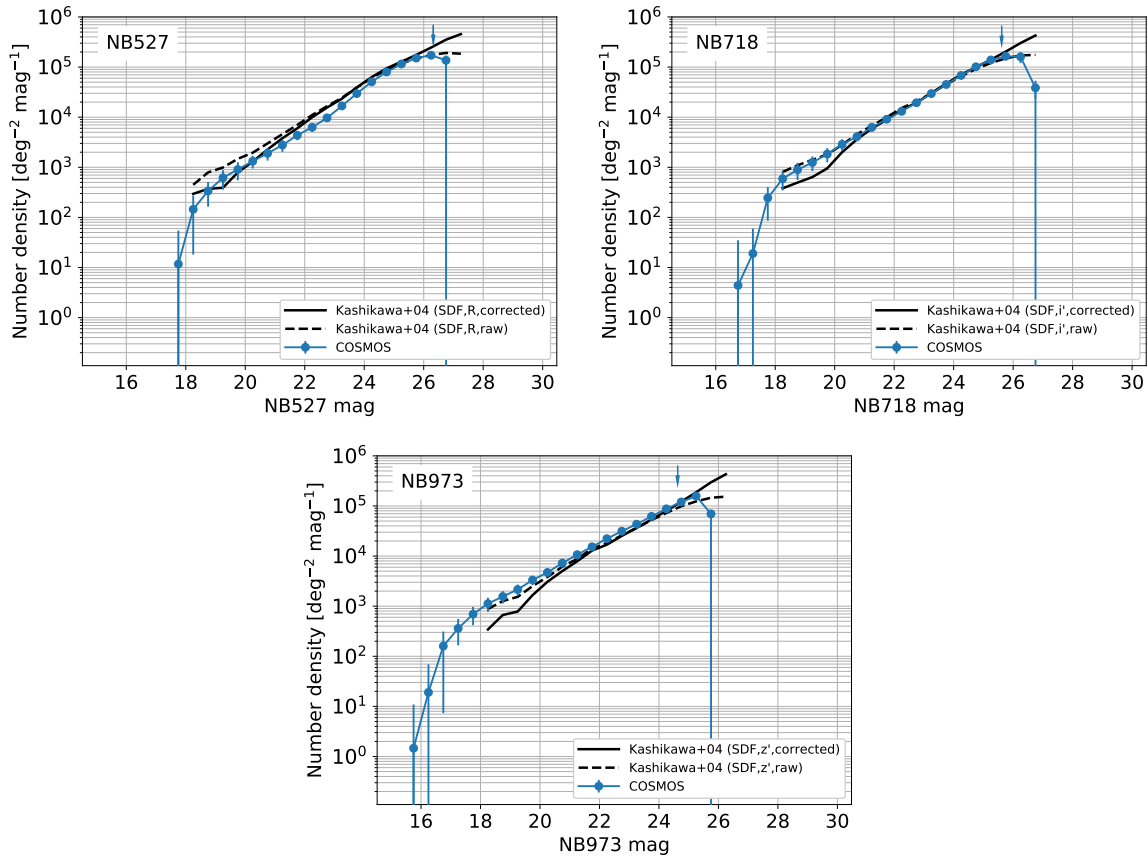


Fig. 18. The same as figure 2, but for the number counts of sources detected in NB527, NB718 and NB973.

Appendix 2 Spatial distribution of emitters

Figures 21 – 23 show the spatial distribution of $H\alpha$, [OIII], and [OII] emission-line galaxies.

References

- Aihara, H., et al. 2018a, PASJ, 70, S8
 —. 2018b, PASJ, 70, S4
 —. 2019, PASJ, 106
 Alam, S., et al. 2015, ApJS, 219, 12
 Baldwin, J. A., Phillips, M. M., & Terlevich, R. 1981, PASP, 93, 5
 Böhm, A., Ziegler, B. L., Pérez-Martínez, J. M., Kodama, T., Hayashi, M., Maier, C., Verdugo, M., & Koyama, Y. 2020, A&A, 633, A131
 Bongiovanni, Á., et al. 2020, A&A, 635, A35
 Bosch, J., et al. 2018, PASJ, 70, S5
 Bradshaw, E. J., et al. 2013, MNRAS, 433, 194
 Bruzual, G., & Charlot, S. 2003, MNRAS, 344, 1000
 Calzetti, D., Armus, L., Bohlin, R. C., Kinney, A. L., Koornneef, J., & Storchi-Bergmann, T. 2000, ApJ, 533, 682
 Cardelli, J. A., Clayton, G. C., & Mathis, J. S. 1989, ApJ, 345, 245
 Chabrier, G. 2003, PASP, 115, 763
 Civano, F., et al. 2016, ApJ, 819, 62
 Coil, A. L., et al. 2011, ApJ, 741, 8
 Cool, R. J., et al. 2013, ApJ, 767, 118
 Cooper, M. C., et al. 2011, ApJS, 193, 14
 —. 2012, MNRAS, 419, 3018
 Coughlin, A., et al. 2018, ApJ, 858, 96
 Coupon, J., Czakon, N., Bosch, J., Komiyama, Y., Medezinski, E., Miyazaki, S., & Oguri, M. 2018, PASJ, 70, S7
 Cucciati, O., et al. 2012, A&A, 539, A31
 Daddi, E., et al. 2007, ApJ, 670, 156
 Dahlen, T., Mobasher, B., Dickinson, M., Ferguson, H. C., Giavalisco, M., Kretchmer, C., & Ravindranath, S. 2007, ApJ, 654, 172
 Dale, D. A., et al. 2010, ApJL, 712, L189
 Davis, M., et al. 2003, in Proc. SPIE, Vol. 4834, Discoveries and Research Prospects from 6- to 10-Meter-Class Telescopes II, ed. P. Guhathakurta, 161–172
 Delvecchio, I., et al. 2017, A&A, 602, A3
 Drake, A. B., et al. 2013, MNRAS, 433, 796
 Drinkwater, M. J., et al. 2010, MNRAS, 401, 1429
 Elbaz, D., et al. 2007, A&A, 468, 33
 Furusawa, H., et al. 2018, PASJ, 70, S3
 Garilli, B., et al. 2014, A&A, 562, A23
 Gruppioni, C., et al. 2013, MNRAS, 432, 23
 Harish, S., et al. 2020, ApJ, 892, 30

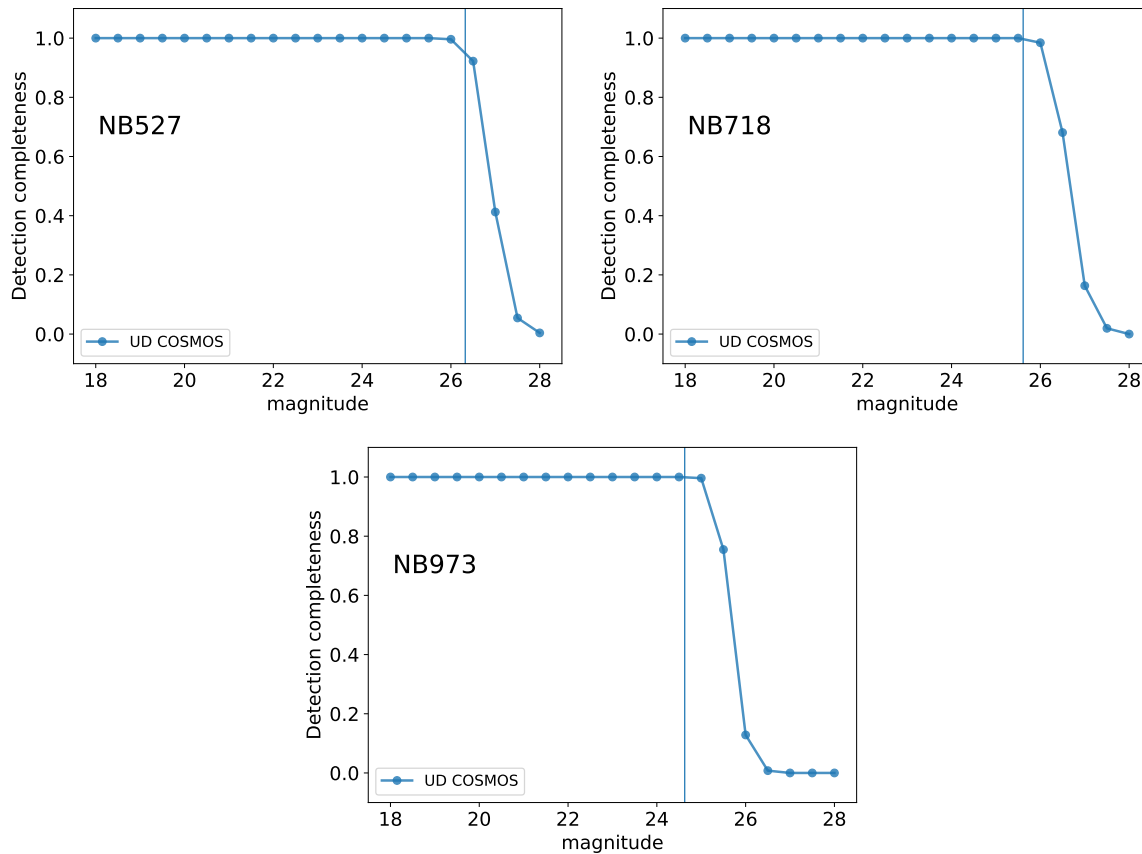


Fig. 19. The same as figure 3, but for the detection completeness for NB527, NB718 and NB973 filters.

- Hasinger, G., et al. 2018, *ApJ*, 858, 77
- Hayashi, M., Sobral, D., Best, P. N., Smail, I., & Kodama, T. 2013, *MNRAS*, 430, 1042
- Hayashi, M., et al. 2015, *PASJ*, 67, 80
- . 2018, *PASJ*, 70, S17
- . 2019, *PASJ*, 71, 112
- Hopkins, A. M., & Beacom, J. F. 2006, *ApJ*, 651, 142
- Inoue et al. 2020, in prep.
- Kashikawa, N., et al. 2002, *PASJ*, 54, 819
- . 2004, *PASJ*, 56, 1011
- Kashino, D., et al. 2019, *ApJS*, 241, 10
- Kawanomoto, S., et al. 2018, *PASJ*, 70, 66
- Kennicutt, Jr., R. C. 1998, *ARA&A*, 36, 189
- Kewley, L. J., Geller, M. J., & Jansen, R. A. 2004, *AJ*, 127, 2002
- Khostovan, A. A., Sobral, D., Mobasher, B., Best, P. N., Smail, I., Stott, J. P., Hemmati, S., & Nayyeri, H. 2015, *MNRAS*, 452, 3948
- Khostovan, A. A., Sobral, D., Mobasher, B., Smail, I., Darvish, B., Nayyeri, H., Hemmati, S., & Stott, J. P. 2016, *MNRAS*, 463, 2363
- Khostovan, A. A., et al. 2018, *MNRAS*, 478, 2999
- . 2020, *MNRAS*
- Komiyama, Y., et al. 2018, *PASJ*, 70, S2
- Konno, A., Ouchi, M., Nakajima, K., Duval, F., Kusakabe, H., Ono, Y., & Shimasaku, K. 2016, *ApJ*, 823, 20
- Koyama, Y., et al. 2018, *PASJ*, 70, S21
- Laigle, C., et al. 2016, *ApJS*, 224, 24
- Le Fèvre, O., et al. 2013, *A&A*, 559, A14
- Lee, J. C., et al. 2012, *PASP*, 124, 782
- Lewis, I. J., et al. 2002, *MNRAS*, 333, 279
- Lilly, S. J., et al. 2009, *ApJS*, 184, 218
- Liske, J., et al. 2015, *MNRAS*, 452, 2087
- Ly, C., Lee, J. C., Dale, D. A., Momcheva, I., Salim, S., Staudaher, S., Moore, C. A., & Finn, R. 2011, *ApJ*, 726, 109
- Ly, C., Malkan, M. A., Kashikawa, N., Hayashi, M., Nagao, T., Shimasaku, K., Ota, K., & Ross, N. R. 2012, *ApJ*, 757, 63
- Ly, C., et al. 2007, *ApJ*, 657, 738
- Madau, P., & Dickinson, M. 2014, *ARA&A*, 52, 415
- Magnelli, B., Elbaz, D., Chary, R. R., Dickinson, M., Le Borgne, D., Frayer, D. T., & Willmer, C. N. A. 2011, *A&A*, 528, A35
- Magnelli, B., et al. 2013, *A&A*, 553, A132
- Marchesi, S., et al. 2016, *ApJ*, 817, 34
- Matsuoka, Y., et al. 2018, *ApJS*, 237, 5
- Matthee, J., Sobral, D., Best, P., Smail, I., Bian, F., Darvish, B., Röttgering, H., & Fan, X. 2017, *MNRAS*, 471, 629
- McLure, R. J., et al. 2013, *MNRAS*, 428, 1088
- Miyazaki, S., et al. 2018, *PASJ*, 70, S1
- Momcheva, I. G., et al. 2016, *ApJS*, 225, 27

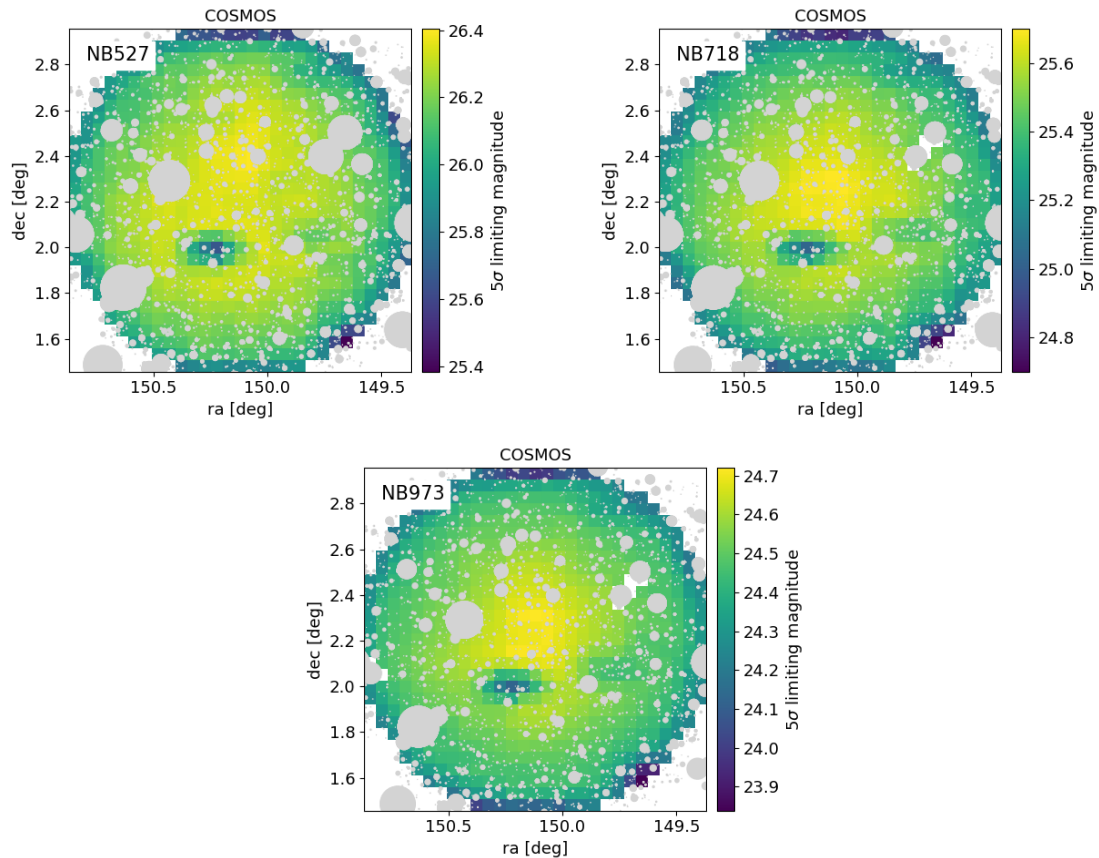


Fig. 20. The same as figure 4, but for the map of 5σ limiting magnitudes in NB527, NB718 and NB973.

- Moustakas, J., Kennicutt, Jr., R. C., & Tremonti, C. A. 2006, *ApJ*, 642, 775
- Nadolny, J., et al. 2020, *A&A*, 636, A84
- Nakajima, K., et al. 2012, *ApJ*, 745, 12
- Newman, J. A., et al. 2013, *ApJS*, 208, 5
- Nishizawa, A. J., Hsieh, B.-C., Tanaka, M., & Takata, T. 2020, arXiv e-prints, arXiv:2003.01511
- Noeske, K. G., et al. 2007, *ApJL*, 660, L43
- Ogura, K., et al. 2020, *ApJ*, 895, 9
- Oke, J. B., & Gunn, J. E. 1983, *ApJ*, 266, 713
- Osterbrock, D. E. 1989, *Astrophysics of gaseous nebulae and active galactic nuclei*
- Pâris, I., et al. 2018, *A&A*, 613, A51
- Paulino-Afonso, A., Sobral, D., Darvish, B., Ribeiro, B., Stroe, A., Best, P., Afonso, J., & Matsuda, Y. 2018, *A&A*, 620, A186
- Peng, Y.-j., et al. 2010, *ApJ*, 721, 193
- Ramón-Pérez, M., et al. 2019a, *A&A*, 631, A10
- . 2019b, *A&A*, 631, A11
- Reddy, N. A., & Steidel, C. C. 2009, *ApJ*, 692, 778
- Robotham, A. S. G., & Driver, S. P. 2011, *MNRAS*, 413, 2570
- Rodighiero, G., et al. 2011, *ApJL*, 739, L40
- Sanders, D. B., Mazzarella, J. M., Kim, D. C., Surace, J. A., & Soifer, B. T. 2003, *AJ*, 126, 1607
- Schechter, P. 1976, *ApJ*, 203, 297
- Schimminovich, D., et al. 2005, *ApJL*, 619, L47
- Scoville, N., et al. 2007, *ApJS*, 172, 1
- Sharp, R., et al. 2006, *Society of Photo-Optical Instrumentation Engineers (SPIE) Conference Series*, Vol. 6269, Performance of AAOmega: the AAT multi-purpose fiber-fed spectrograph, 62690G
- Shibuya, T., et al. 2018, *PASJ*, 70, S15
- Silverman, J. D., et al. 2015, *ApJS*, 220, 12
- Skelton, R. E., et al. 2014, *ApJS*, 214, 24
- Sobral, D., Best, P. N., Matsuda, Y., Smail, I., Geach, J. E., & Cirasuolo, M. 2012, *MNRAS*, 420, 1926
- Sobral, D., Best, P. N., Smail, I., Geach, J. E., Cirasuolo, M., Garn, T., & Dalton, G. B. 2011, *MNRAS*, 411, 675
- Sobral, D., Best, P. N., Smail, I., Mobasher, B., Stott, J., & Nisbet, D. 2014, *MNRAS*, 437, 3516
- Sobral, D., Kohn, S. A., Best, P. N., Smail, I., Harrison, C. M., Stott, J., Calhau, J., & Matthee, J. 2016a, *MNRAS*, 457, 1739
- Sobral, D., Santos, S., Matthee, J., Paulino-Afonso, A., Ribeiro, B., Calhau, J., & Khostovan, A. A. 2018, *MNRAS*, 476, 4725
- Sobral, D., Smail, I., Best, P. N., Geach, J. E., Matsuda, Y., Stott, J. P., Cirasuolo, M., & Kurk, J. 2013, *MNRAS*, 428, 1128
- Sobral, D., Stroe, A., Koyama, Y., Darvish, B., Calhau, J.,

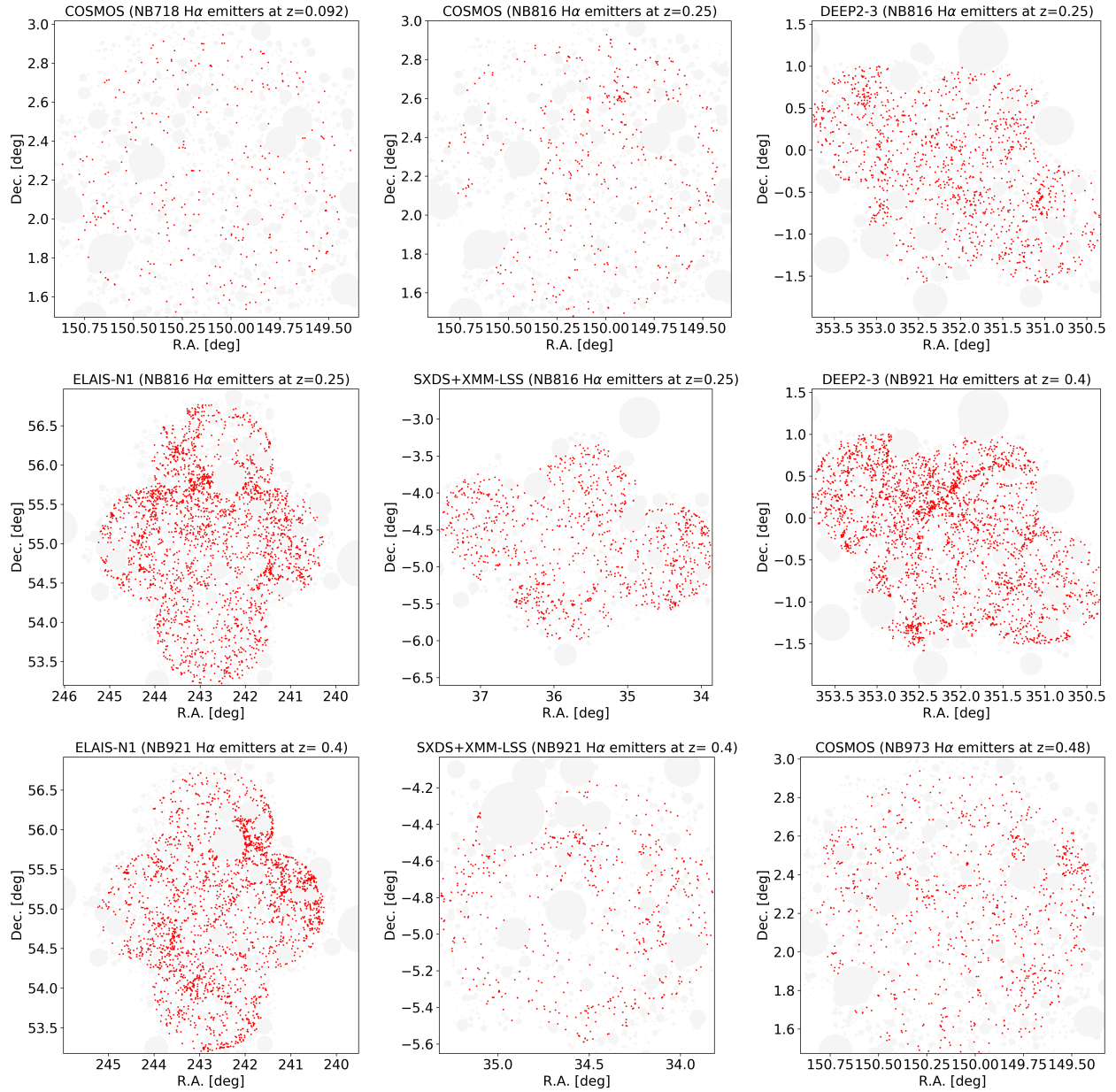


Fig. 21. The spatial distribution of H α emission-line galaxies.

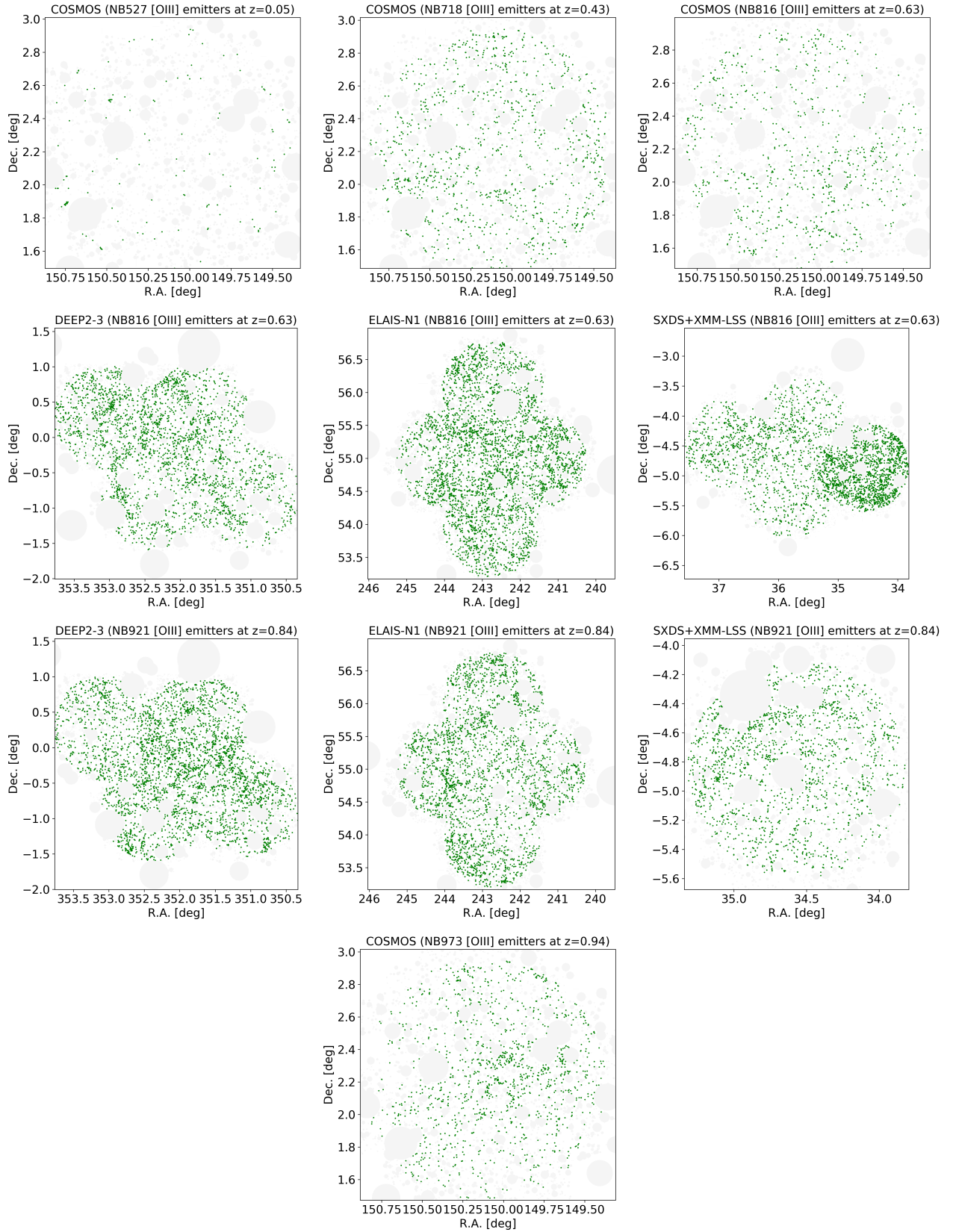


Fig. 22. The spatial distribution of [OIII] emission-line galaxies.

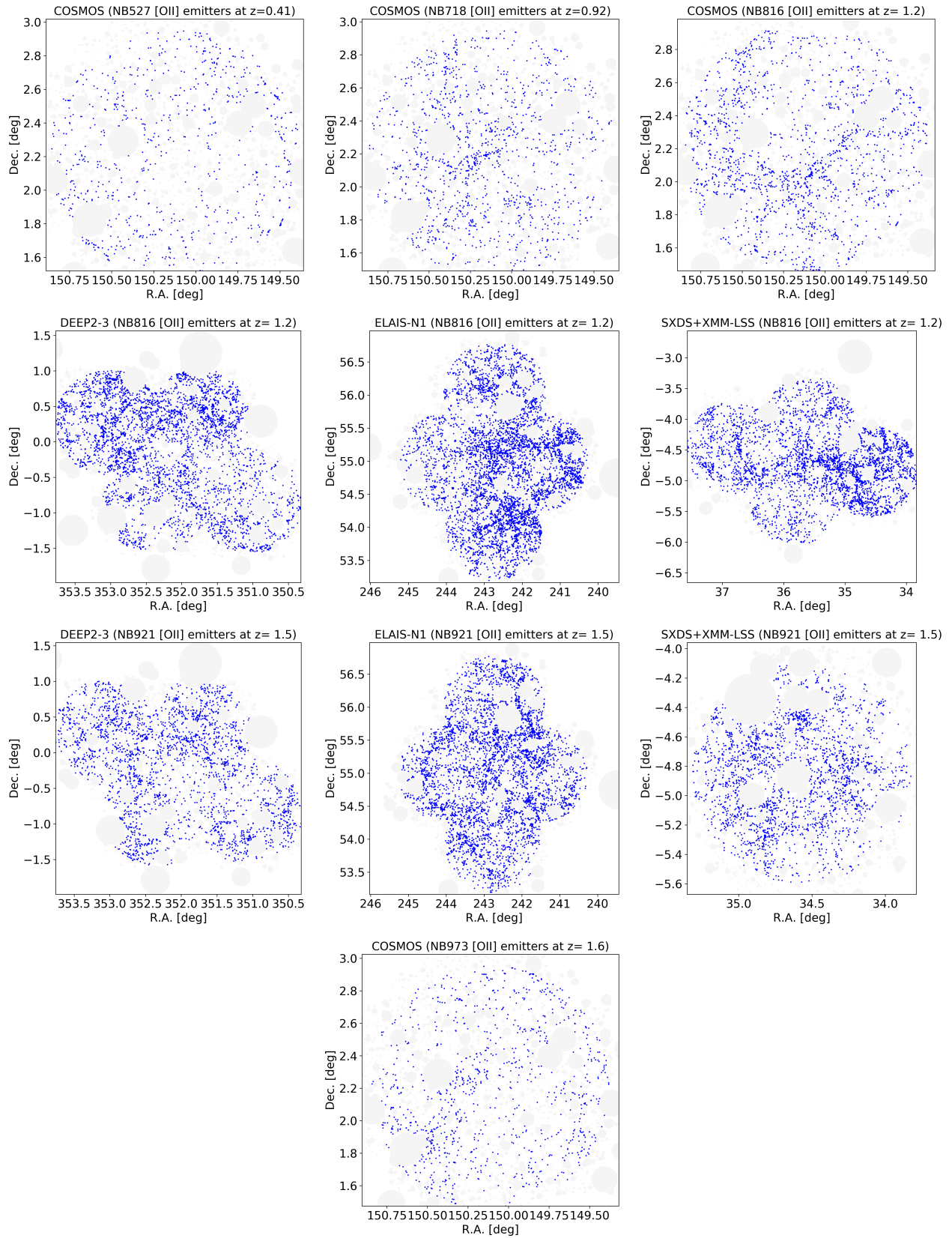


Fig. 23. The spatial distribution of [OII] emission-line galaxies.

- Afonso, A., Kodama, T., & Nakata, F. 2016b, *MNRAS*, 458, 3443
- Sobral, D., et al. 2009, *MNRAS*, 398, 75
- . 2015, *MNRAS*, 451, 2303
- . 2017, *MNRAS*, 466, 1242
- Speagle, J. S., Steinhardt, C. L., Capak, P. L., & Silverman, J. D. 2014, *ApJS*, 214, 15
- Stroe, A., & Sobral, D. 2015, *MNRAS*, 453, 242
- Stroe, A., Sobral, D., Matthee, J., Calhau, J., & Oteo, I. 2017a, *MNRAS*, 471, 2558
- Stroe, A., Sobral, D., Paulino-Afonso, A., Alegre, L., Calhau, J., Santos, S., & van Weeren, R. 2017b, *MNRAS*, 465, 2916
- Stroe, A., Sobral, D., Röttgering, H. J. A., & van Weeren, R. J. 2014, *MNRAS*, 438, 1377
- Stroe, A., et al. 2015, *MNRAS*, 450, 646
- Takeuchi, T. T., Yoshikawa, K., & Ishii, T. T. 2003, *ApJL*, 587, L89
- Tanaka, M. 2015, *ApJ*, 801, 20
- Tanaka, M., et al. 2018, *PASJ*, 70, S9
- Tomczak, A. R., et al. 2016, *ApJ*, 817, 118
- Vilella-Rojo, G., et al. 2015, *A&A*, 580, A47
- Whitaker, K. E., et al. 2014, *ApJ*, 795, 104
- Wyder, T. K., et al. 2005, *ApJL*, 619, L15
- Yuan, F., et al. 2015, *MNRAS*, 452, 3047